Article

Cell Reports

Shootin1b Mediates a Mechanical Clutch to Produce Force for Neuronal Migration

Graphical Abstract

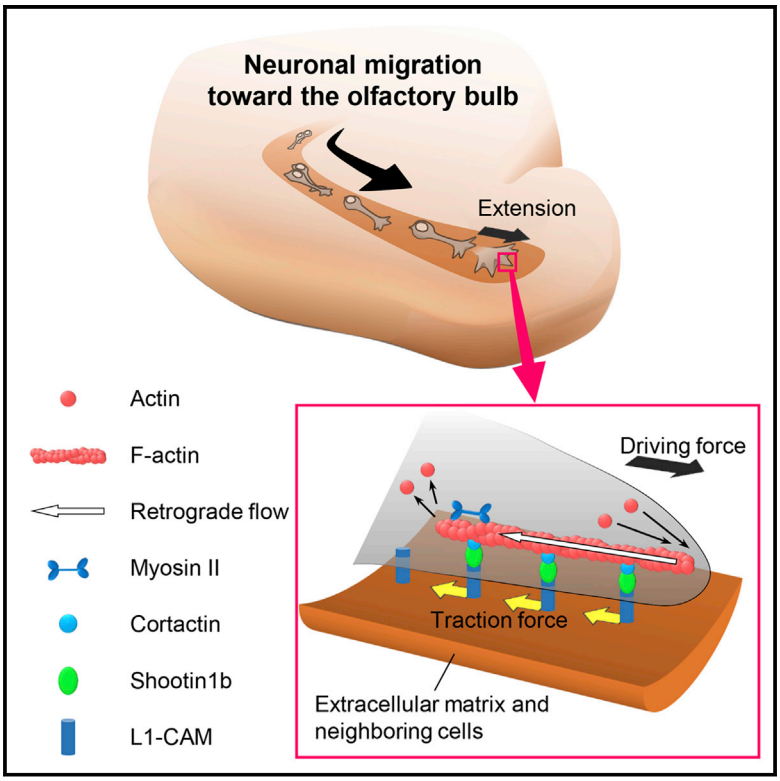

Highlights

- Shootin1b accumulates at the leading process growth cone of olfactory interneurons
- Shootin1b couples F-actin retrograde flow and cell adhesions as a clutch molecule
- The shootin1b-mediated clutch coupling generates force for neuronal migration
- Loss of shootin1 inhibits rostral migration of olfactory interneurons in the brain

Authors

Takunori Minegishi, Yasuyuki Uesugi, Naoko Kaneko, Wataru Yoshida, Kazunobu Sawamoto, Naoyuki Inagaki

Correspondence

ninagaki@bs.naist.jp

In Brief

Minegishi et al. use gene knockout, protein interaction assays, force microscopy, speckle imaging, and migration assays to analyze the molecular mechanics driving neuronal migration *in vivo*. Their data demonstrate that shootin1b mediates a mechanical clutch to produce force for the migration of olfactory interneurons in the brain.

Minegishi et al., 2018, Cell Reports *25*, 624–639
October 16, 2018
https://doi.org/10.1016/j.celrep.2018.09.068

CellPress

OPEN ACCESS
CellPress

Cell Reports
Article

Shootin1b Mediates a Mechanical Clutch to Produce Force for Neuronal Migration

Takunori Minegishi,[1] Yasuyuki Uesugi,[1] Naoko Kaneko,[2] Wataru Yoshida,[1] Kazunobu Sawamoto,[2,3] and Naoyuki Inagaki[1,4,*]

[1]Laboratory of Systems Neurobiology and Medicine, Division of Biological Science, Nara Institute of Science and Technology, Ikoma, Nara 630-0192, Japan

[2]Department of Developmental and Regenerative Biology, Graduate School of Medical Sciences, Nagoya City University, Nagoya 467-8601, Japan

[3]Division of Neural Development and Regeneration, National Institute for Physiological Sciences, Okazaki 444-8585, Japan

[4]Lead Contact

*Correspondence: ninagaki@bs.naist.jp

https://doi.org/10.1016/j.celrep.2018.09.068

SUMMARY

As an essential step for brain morphogenesis, neurons migrate via mechanical interactions with components of their environment such as neighboring cells and the extracellular matrix. However, the molecular mechanism by which neurons exert forces on their environment during migration remains poorly understood. Here, we show that shootin1b is expressed in migrating mouse olfactory interneurons and accumulates at their leading process growth cone. We demonstrate that shootin1b, by binding to cortactin and L1-CAM, couples F-actin retrograde flow and the adhesive substrate as a clutch molecule. Shootin1b-mediated clutch coupling at the growth cone generates traction force on the substrate, thereby promoting leading process extension and subsequent somal translocation of olfactory interneurons. Furthermore, loss of shootin1 causes abnormal positioning of the interneurons and dysgenesis of the olfactory bulb. Our findings indicate that shootin1b plays a key role in force-driven leading process extension, which propels the migration of olfactory interneurons during olfactory bulb formation.

INTRODUCTION

Neuronal migration is an essential process for the proper formation of brain architecture and neuronal networks (Marín and Rubenstein, 2003; Ayala et al., 2007). Defects in neuronal migration are associated with a number of diseases including brain malformation, mental retardation, epilepsy, and psychiatric disorders (Ayala et al., 2007; Evsyukova et al., 2013). Among the migration modes of various cell types, a unique feature in neurons is that they extend a long leading process: neurons migrate in a saltatory manner that includes leading process extension and somal translocation (Marín et al., 2010; Cooper, 2013; Kaneko et al., 2017). The leading process plays a pivotal role in neuronal migration (He et al., 2010; Cooper, 2013); the molecular bases underlying somal translocation have also been reported (Marín et al., 2010; Solecki, 2012; Cooper, 2013; Evsyukova et al., 2013; Kaneko et al., 2017). During migration, force generated within the leading process is thought to pull the centrosome forward (Marín et al., 2010). Perinuclear microtubules (Rivas and Hatten, 1995) pull the nucleus to the anterior-located centrosome supported by dynein motors and related molecules, such as Lissencephaly 1 and Doublecortin (Shu et al., 2004; Tanaka et al., 2004; Tsai and Gleeson, 2005; Marín et al., 2010). Actomyosin at the rear additionally contributes to somal translocation in a RhoA-dependent manner (Bellion et al., 2005; Schaar and McConnell, 2005; Martini and Valdeolmillos, 2010; Shinohara et al., 2012). On the other hand, cell migrations also require mechanical interactions with components of their environment including neighboring cells and the extracellular matrix (Gardel et al., 2010; Charras and Sahai, 2014). However, little is known about the molecular mechanism by which neurons exert forces on their environment to drive cell migration.

Clutch molecules play key roles in driving axon outgrowth and guidance. In the axonal growth cone, actin filament (F-actin) networks polymerize at the leading edge and disassemble proximally (Suter and Forscher, 2000; Pollard and Borisy, 2003; Lowery and Van Vactor, 2009), which, in conjunction with myosin II activity, induces retrograde flow of F-actins (Suter and Forscher, 2000; Medeiros et al., 2006). Mechanical coupling between the F-actin retrograde flow and cell-adhesion molecules by clutch molecules transmits the force of F-actin flow to the adhesive substrate, thereby generating the traction force to propel axonal growth cone migration (Mitchison and Kirschner, 1988; Suter and Forscher, 2000; Bard et al., 2008; Chan and Odde, 2008; Shimada et al., 2008; Lowery and Van Vactor, 2009; Garcia et al., 2015; Baba et al., 2018). Previous studies with migratory cerebellar granule cells reported F-actin retrograde flow (He et al., 2010) and traction force (Jiang et al., 2015) at the leading process growth cone. However, whether clutch molecules are utilized in neuronal cell migration remains unknown. In addition, it is proposed that the mechanisms underlying neuronal cell migration may be distinct from those involved in axon guidance (Marín et al., 2010). Furthermore, recent studies have reported a wide range of alternative migration modes for non-neuronal cells in three-dimensional (3D) environments that may not involve F-actin-adhesion coupling (Lämmermann et al., 2008; Petrie et al., 2014; Stroka et al., 2014), thereby raising the question of whether cells *in vivo* generally utilize a clutch molecule for migration.

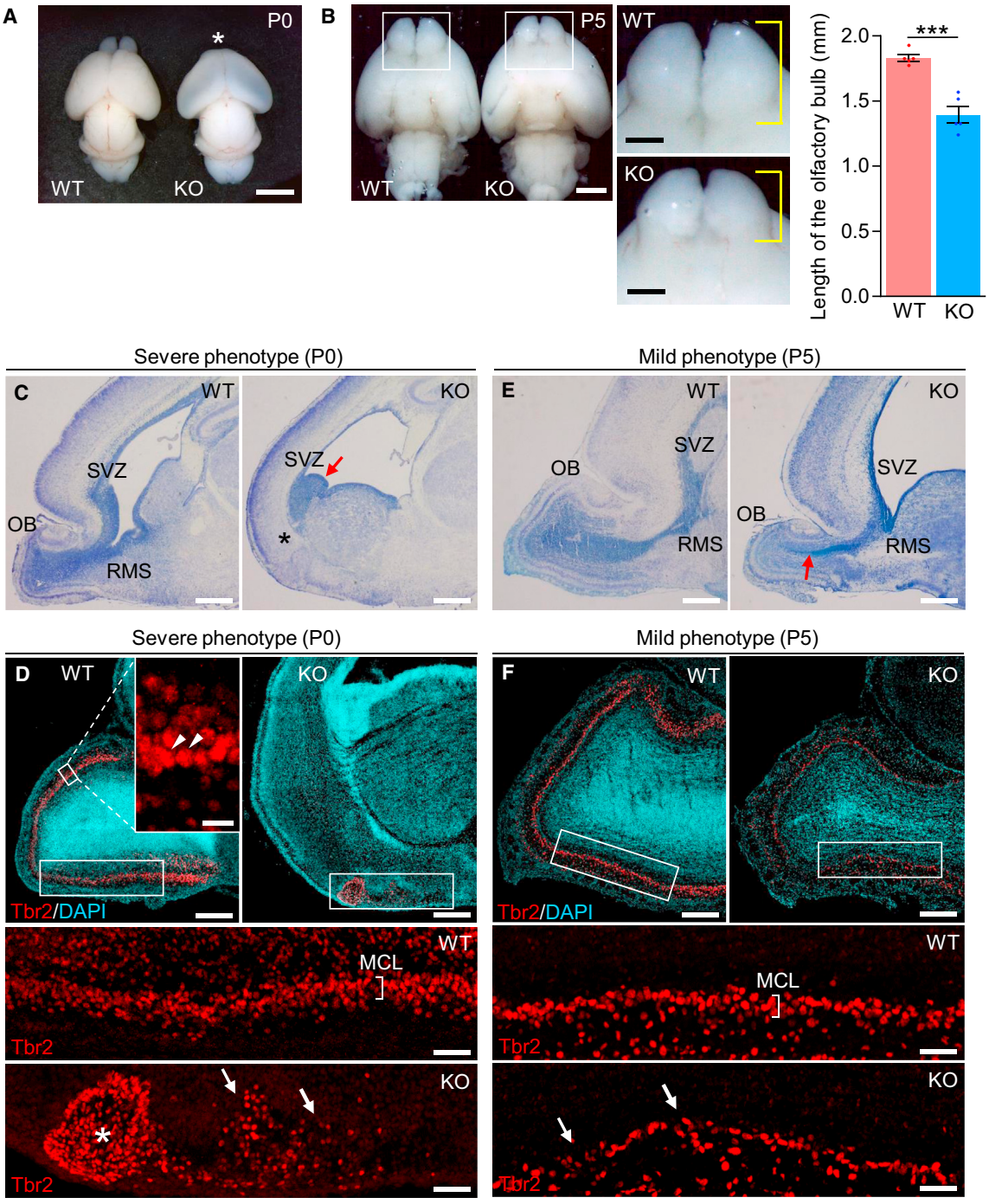

Figure 1. Loss of Shootin1 Causes Dysgenesis of the Olfactory Bulb and Abnormal Positioning of Olfactory Neurons

(A) Top view of the brains of a WT mouse and a shootin1 KO mouse exhibiting agenesis of the olfactory bulb (asterisk, severe phenotype) at P0.

(B) Bottom view of the brains of a WT mouse and a shootin1 KO mouse exhibiting a smaller olfactory bulb (mild phenotype) at P5. Right images are enlargements of the regions indicated by boxes. Brackets show the length of the olfactory bulb. The right graph shows a statistical analysis of the length of the olfactory bulb. Two-tailed unpaired Student's t test, p = 0.00101, $t_{(8)}$ = 6.48 (n: 5 WT brains; 5 KO brains).

(C–F) Histological analyses of shootin1 KO mouse brains exhibiting the severe phenotype at P0 (C and D) and mild phenotype at P5 (E and F). OB, olfactory bulb. RMS, rostral migratory stream. SVZ, subventricular zone. MCL, mitral cell layer.

(C and E) Nissl staining of sagittal sections. The asterisk in (C) indicates the putative position of the RMS. Arrows in (C) and (E) indicate abnormal accumulation of cells in the SVZ and the reduction of cell number in the distal part of the RMS, respectively.

(legend continued on next page)

Olfactory interneurons provide an excellent system to analyze neuronal migration in the developing and adult brain (Marín et al., 2010; Lim and Alvarez-Buylla, 2016; Kaneko et al., 2017). In the developing olfactory bulb, the precursors of excitatory projection neurons are thought to migrate radially from the ventricular zone and to form the mitral cell layer (Hinds, 1968; Blanchart et al., 2006). On the other hand, the precursors of interneurons, generated in the dorsal region of the lateral ganglionic eminence (LGE), migrate tangentially to the olfactory bulb (Marín and Rubenstein, 2001; Ayala et al., 2007; Lledo et al., 2008). In contrast to most of other brain regions, the olfactory bulb continuously receives a new supply of interneurons for renewal from the subventricular zone (SVZ) after birth (Ghashghaei et al., 2007; Lledo et al., 2008; Belvindrah et al., 2009; Lim and Alvarez-Buylla, 2016). These postnatal interneurons, called SVZ neuroblasts, migrate through a highly restricted route termed the rostral migratory stream (RMS) (Marín and Rubenstein, 2003; Lledo et al., 2008; Kaneko et al., 2017).

Shootin1a (Toriyama et al., 2006; Higashiguchi et al., 2016) functions as an axonal clutch molecule: it accumulates at the leading edge of the axonal growth cone and couples F-actin retrograde flow and the transmembrane cell-adhesion molecule L1-CAM (Rathjen and Schachner, 1984), producing traction force for axon outgrowth (Shimada et al., 2008; Kubo et al., 2015) and guidance (Abe et al., 2018; Baba et al., 2018). We recently identified shootin1b, a splicing isoform of shootin1a, which is expressed in both the brain and peripheral tissues (Higashiguchi et al., 2016). Here, we analyzed the function of shootin1b in the brain. We show that shootin1b is expressed at high levels along the migratory route of mouse olfactory interneurons and accumulates at the growth cones of their leading process; this accumulation positively correlates with leading process extension. We demonstrate that shootin1b at the leading process growth cone couples F-actin retrograde flow and cell adhesions via the F-actin-interacting protein cortactin (Weed and Parsons, 2001) and the cell-adhesion molecule L1-CAM (Rathjen and Schachner, 1984; Kamiguchi et al., 1998), thereby generating traction force on the adhesive substrate. The olfactory interneurons of shootin1 knockout (KO) mice showed impaired leading process extension and disturbed rostral migration toward the olfactory bulb. Moreover, shootin1 KO reduced the number of cells in the distal RMS. Together, our data indicate that shootin1b constitutes the clutch machinery to drive the leading process extension and tangential migration of olfactory interneurons.

RESULTS

Loss of Shootin1 Causes Dysgenesis of the Olfactory Bulb and Abnormal Positioning of Olfactory Neurons

To study the role of shootin1 in brain development, we analyzed shootin1 KO mice (Baba et al., 2018) and found that they exhibited impaired formation of the olfactory bulb. As a severe phenotype, 35% (n = 26) of postnatal day 0 (P0) shootin1 KO mice displayed agenesis of the olfactory bulb (asterisk, Figure 1A). The other 65% showed apparently normal morphology of the olfactory bulb at birth; however, 20% of P5 shootin1 KO mice that had the olfactory bulb (n = 60) showed a 24% reduction in its length, as a mild phenotype (Figure 1B). Histological analysis of P0 shootin1 KO mouse brains lacking the olfactory bulb revealed agenesis of the RMS (asterisk, Figure 1C) and abnormal accumulation of cells in the SVZ (arrow, Figure 1C), where LGE-derived stem cells generate the majority of postnatal olfactory interneuron precursors (Young et al., 2007). We also labeled the olfactory projection neurons, mitral cells, using an antibody to the specific marker Tbr2 (Besse et al., 2011) (Figure 1D); these cells had a large and round Tbr2-positive nucleus, which is a characteristic feature of mitral cells (Besse et al., 2011) (arrowheads, inset). In brains with the severe phenotype, mitral cells did not form a typical mitral cell layer (arrows, Figure 1D) and assembled ectopically at the ventral forebrain region (asterisk, Figure 1D). In brains with the mild phenotype, we observed a reduced number of cells in the olfactory bulb distal to the RMS on P5 (arrow, Figure 1E) and moderate disorganization of the mitral cell layer (arrows, Figure 1F). Together, these results indicate that shootin1 is required for the formation and growth of the olfactory bulb as well as normal positioning of the olfactory neurons.

Shootin1b Is Expressed in Migrating Olfactory Interneurons and Highly Accumulated at Their Leading Process Growth Cone

The *Shootin1* gene expresses two splicing isoforms, shootin1a and shootin1b (Higashiguchi et al., 2016) (Figure S1). To examine whether these isoforms are expressed in the olfactory bulb, we performed immunohistochemistry using antibodies that specifically recognize shootin1a and shootin1b, respectively (Figure 2A). On P0, high levels of shootin1b immunolabeling were detected in the migratory route of olfactory interneurons, including the SVZ, RMS, and the extension of the RMS in the olfactory bulb (OB-RMS), whereas we detected prominent shootin1a immunoreactivity in the outer region including the mitral cell layer (Figure 2B). We further examined shootin1b expression at different developmental stages. On E12.5, the LGE, where olfactory interneurons are born (Tucker et al., 2006), is morphologically distinguishable (Bulfone et al., 1993); shootin1b immunolabeling was detected in the LGE at this stage (asterisks, Figure S2A) but not in the olfactory bulb primordium (arrowheads). On E14.5, olfactory interneurons start their migration toward the olfactory bulb (Tucker et al., 2006); prominent immunolabeling of shootin1b was detected in the LGE (asterisks, Figure S2B) and the migratory route at this stage (arrowheads). On E16.5, high levels of shootin1b immunolabeling were observed in the migratory route, which is expanding toward the olfactory bulb (arrowheads, Figure S2C).

(D and F) Sagittal sections labeled with anti-Tbr2 antibody (red) and DAPI (cyan). Arrowheads in the inset in (D) show large and round Tbr2-positive nuclei, which are a characteristic feature of mitral cells. Regions in the four large rectangles are shown below as enlarged images. Arrows and the asterisk indicate, respectively, neurons that did not form a typical mitral cell layer and that assembled ectopically.

Data represent means ± SEM. ***$p < 0.01$. Scale bars: 2 mm for (A) and (B, left), 1 mm for (B, right), 400 μm for (C) and (E), 200 μm for (D, top, main images) and (F, top), 50 μm for (D, middle, bottom) and (F, middle, bottom), and 20 μm for (D, inset).

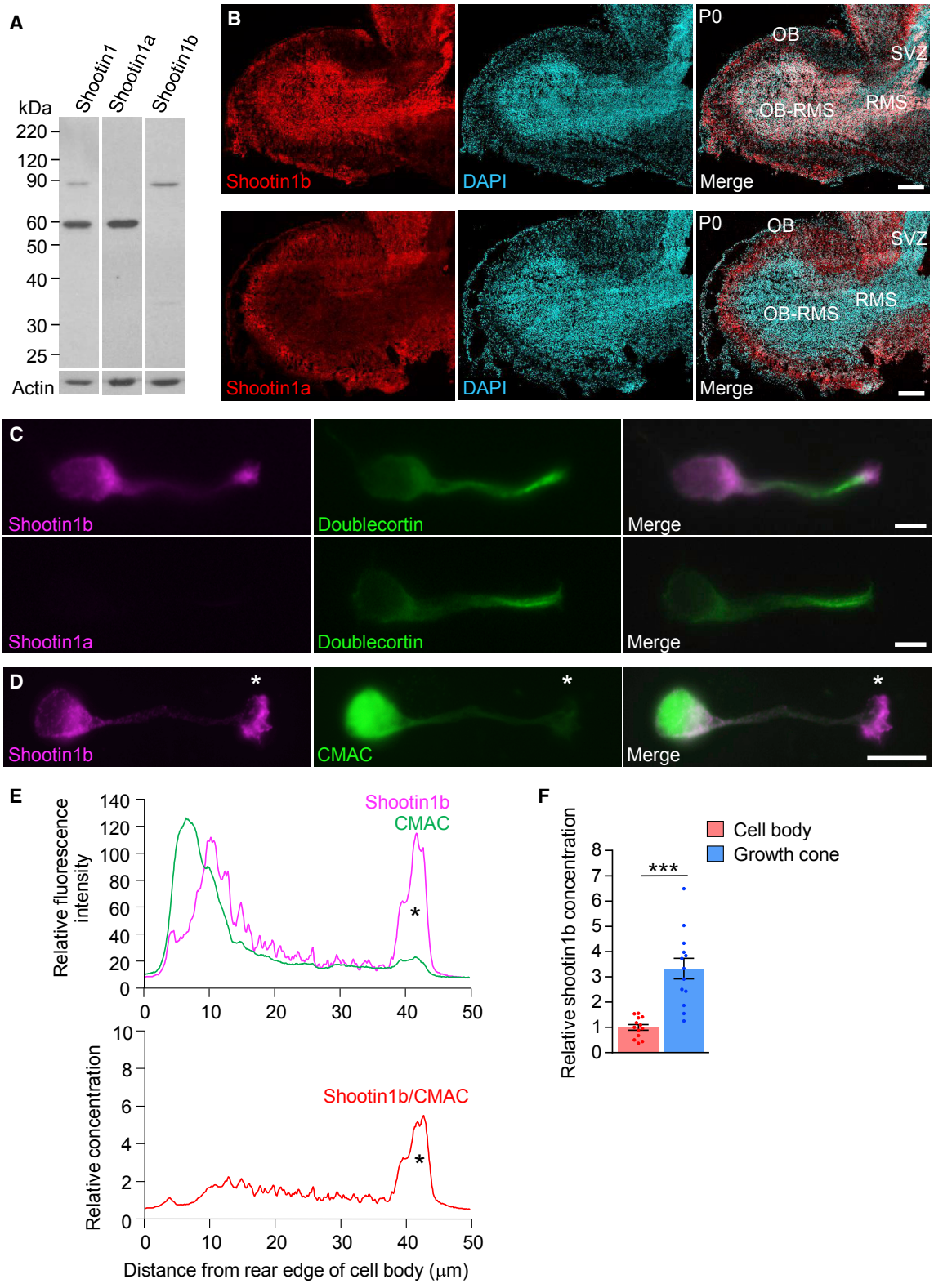

(legend on next page)

Consistent with these immunohistochemical data, shootin1b, but not shootin1a, was detected in doublecortin-positive neuroblasts cultured from the anterior region of the P5 SVZ (Figures 2C and S2D). The intracellular localization of shootin1b in these cells was analyzed by quantifying the signals of shootin1b, together with that of the volume marker CMAC (7-amino-4-chloromethylcoumarin) (Figure 2D). The concentration profile of shootin1b (shootin1b/CMAC) was roughly flat along the cell body and the shaft of the leading processes, but showed a prominent peak at the leading edge, the growth cone (Cooper, 2013), of the leading process (asterisks, Figure 2E). The relative shootin1b concentration in the growth cone was 3.3 times higher than that in the cell body (Figure 2F). Together, these results indicate that shootin1b is preferentially expressed in migrating olfactory interneurons and accumulates highly at their leading process growth cone.

Shootin1b Mediates Rostral Migration of Olfactory Interneurons

The expression of shootin1b in olfactory interneurons (Figure 2), together with the reduced number of cells in the distal RMS of shootin1 KO mice (arrow, Figure 1E), raises the possibility that shootin1b may mediate the migration of olfactory interneurons. To examine this possibility, we next analyzed the migration of olfactory interneurons in the SVZ-RMS-olfactory bulb pathway. Neuroblasts isolated from the SVZ of P2–P5 wild-type (WT) mice and from the SVZ of P2–P5 shootin1 KO mice were labeled with the fluorescent dyes PKH-26 and PKH-67, respectively; they were then mixed and injected into the SVZ of P7–P8 WT mice. Two days after the cell transplantation, sagittal sections of the olfactory bulb were prepared. We analyzed the PKH-labeled neurons distributed in the outer layer of the olfactory bulb (OB-Outer), OB-RMS, the anterior part of the RMS (aRMS) and the posterior part of the RMS (pRMS) (Figures S3 and 3A). As shown in Figure 3B, the percentages of neurons that reached OB-Outer and OB-RMS were significantly reduced in shootin1 KO neurons, suggesting that shootin1 KO impairs the rostral migration of olfactory interneurons. We further measured the migration speed of transplanted neuroblasts in the RMS by live imaging (Kaneko et al., 2010; Ota et al., 2014) (Figure 3C; Video S1) and found that it was significantly reduced in shootin1 KO neuroblasts (Figure 3D; WT, 2.12 ± 0.08 μm/min, n = 91 cells; KO, 1.76 ± 0.09 μm/min, n = 70 cells; $p < 0.01$). Thus, these results suggest that shootin1b plays a key role in the rostral migration of olfactory interneurons.

Shootin1b Mediates Leading Process Extension and Somal Translocation of Olfactory Interneurons

To analyze the locomotion steps of olfactory interneurons mediated by shootin1b, we performed live-cell imaging of mRFP-shootin1b using cultured neurons (Figure 4A; Video S2). For observation under 3D conditions, the cells were cultured in a mixture of 75% Matrigel and 25% L-15 medium. Relative shootin1b concentration at the growth cone of leading processes was calculated using the AcGFP signal as an internal standard (mRFP-shootin1b/AcGFP). Shootin1b underwent dynamic accumulation at the growth cone, which is associated with advance and retraction of the growth cone (kymograph, Figure 4A). We quantified the advance speed of the leading process growth cone and relative shootin1 concentration there and found a positive correlation between them ($r = 0.505$, Figure 4B, n = 8 cells).

Figure 4C and Video S3 show representative locomotion steps of WT and shootin1 KO olfactory interneurons within 3D Matrigel. As reported (Wichterle et al., 1997), neuroblasts prepared from WT SVZ (P5) migrated in a saltatory manner that includes the advance of the leading process growth cone and somal translocation, which are associated with extension (blue arrowheads to red arrowheads, Figure 4D) and retraction (red arrowheads to blue arrowheads) of the leading process. Consistent with the data *in vivo* (Figure 3), the speed of somal translocation was significantly reduced in shootin1 KO neuroblasts (Figures 4C and 4E; WT, 0.16 ± 0.03 μm/min, n = 11 cells; KO, 0.06 ± 0.02 μm/min, n = 11 cells; $p < 0.01$). The average length of the leading processes was 38.8 ± 4.0 μm in WT neuroblasts, and it was significantly reduced in shootin1 KO neuroblasts (Figures 4C and 4F). In addition, the range of extension (blue arrowheads to red arrowheads, Figure 4D) and retraction (red arrowheads to blue arrowheads) of leading processes was reduced in shootin1 KO neuroblasts (Figure 4G). On the other hand, the frequency of the extensions/retractions was not statistically different in WT and shootin1 KO neuroblasts (Figure 4H). Expression of shootin1b in shootin1 KO neuroblasts rescued the reductions in the somal translocation speed as well as the length and extension/retraction range of the leading process (Figures 4D–4G).

Figure 2. Expression and Localization of Shootin1b in Olfactory Interneurons

(A) Immunoblot analysis of E18.5 mouse brain lysate (10 μg proteins) with anti-shootin1 (left), anti-shootin1a (middle) and anti-shootin1b (right) antibodies. The anti-shootin1 antibody recognized shootin1a (~60 kDa) and shootin1b (~87 kDa), while the anti-shootin1a and anti-shootin1b antibodies recognized specifically shootin1a and shootin1b, respectively. Immunoblots with anti-actin antibody served as loading controls.

(B) Sagittal sections of P0 mouse brains labeled with anti-shootin1b antibody (red, upper), anti-shootin1a antibody (red, lower), and DAPI (cyan). OB, olfactory bulb. RMS, rostral migratory stream. SVZ, subventricular zone.

(C and D) Shootin1b localization in 2 days *in vitro* (DIV2) neuroblasts prepared from P5 mouse SVZ and cultured on laminin-coated coverslips.

(C) Neuroblasts were stained with anti-shootin1b antibody (magenta, upper), anti-shootin1a antibody (magenta, lower), and anti-doublecortin antibody (green). Anti-doublecortin antibody was used as a marker of neuroblasts.

(D–F) Neuroblasts were stained with anti-shootin1b antibody (magenta) and CMAC (green) (D). CMAC was used as a volume marker. Asterisks indicate the growth cone. Line-scan profiles (E) show the relative fluorescence intensities of shootin1b (magenta) and CMAC (green) and the relative concentration of shootin1b (shootin1b/CMAC, red) from the cell body to the growth cone (asterisks). The relative concentration of shootin1b was compared between the growth cone and the cell body (F). To compare the shootin1b concentration, the fluorescence intensities of shootin1b and CMAC in the same region were measured at the center of the growth cone and at the cell body in front of the nucleus. The relative shootin1b concentrations in each region were calculated and normalized with the average concentration in the cell body. Two-tailed unpaired Welch's t test, $p = 8.04 \times 10^{-5}$, $t_{(14)} = -5.48$ (n = 13 cells).

Data represent means ± SEM. ***$p < 0.01$. Scale bars: 200 μm for (B) and 10 μm for (C) and (D). See also Figures S1 and S2.

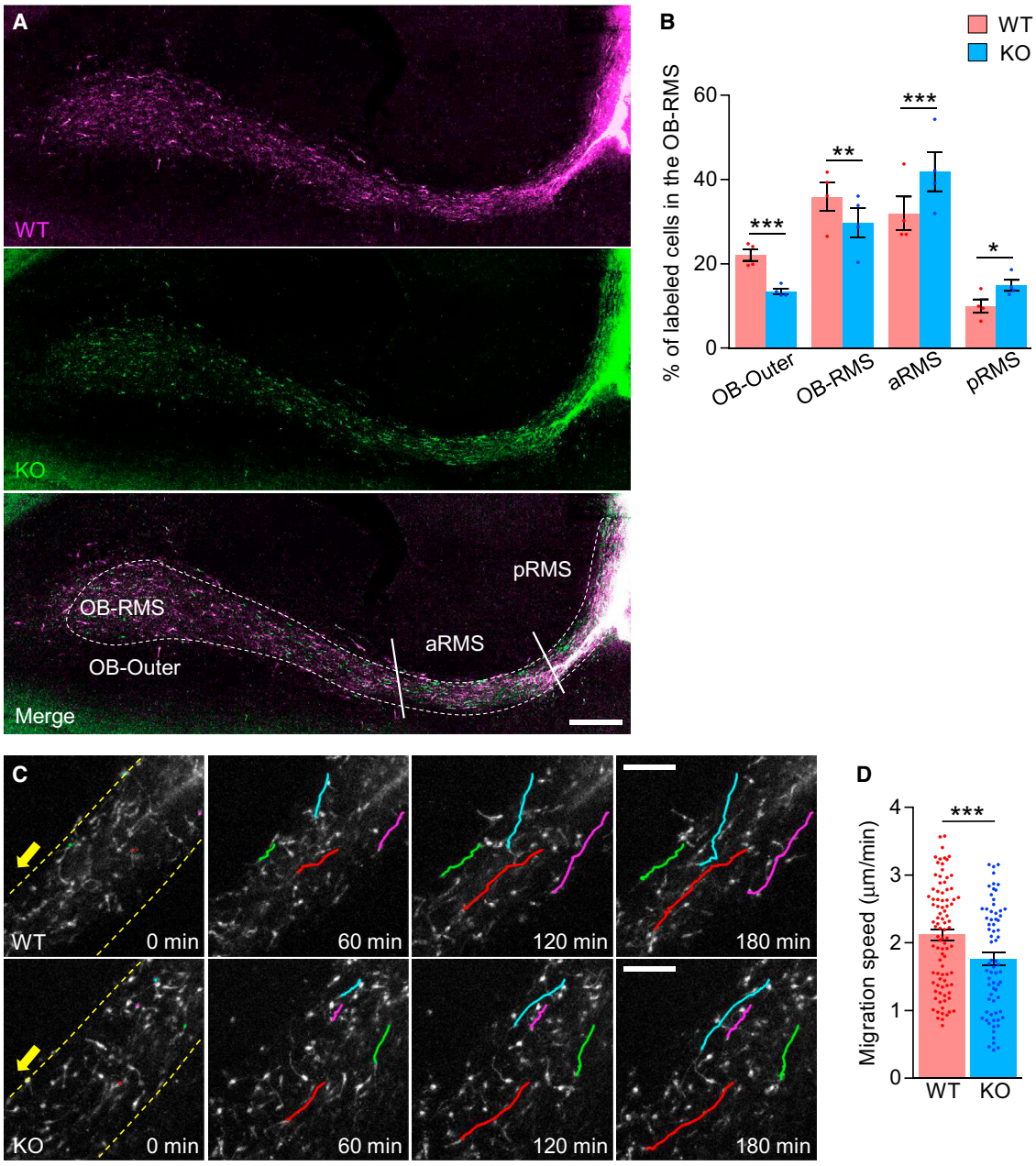

Figure 3. Shootin1 KO Inhibits Rostral Migration of Olfactory Interneurons

(A) Distribution of WT (magenta) and shootin1 KO (green) neuroblasts in the olfactory bulb and RMS. Neuroblasts isolated from the WT and shootin1 KO SVZ were labeled with the fluorescent dyes PKH-26 and PKH-67, respectively, and injected into the SVZ of WT mice. Two days later, sagittal sections of the olfactory bulb were prepared and analyzed. The olfactory bulb and RMS are divided into four regions: pRMS, aRMS, OB-RMS, and OB-outer (see Figure S3).

(B) Quantitative analysis of WT and shootin1 KO neuroblasts distributed in pRMS, aRMS, OB-RMS, and OB-outer. Cells were prepared from 9 WT and 9 shootin1 KO mice (6 mothers) and then transplanted into WT brains (n: 1,656 WT cells and 1,627 shootin1 KO cells counted from 3–5 sections of 4 WT brains). Two-tailed paired t test for each region. OB-outer: $p = 0.00715$, $t_{(3)} = 6.58$. OB-RMS: $p = 0.0101$, $t_{(3)} = 5.83$. aRMS; $p = 0.00969$, $t_{(3)} = -5.91$. pRMS: $p = 0.0214$, $t_{(3)} = -4.43$.

(C) Time-lapse imaging of migrating WT and shootin1 KO neuroblasts in the RMS (see Video S1). Neuroblasts were tracked as shown by colored lines (red, magenta, green, and cyan). Dashed lines indicate the RMS. Arrows indicate the rostral direction of the olfactory bulb.

(D) Migration speed of transplanted neuroblasts in the RMS. Cells were prepared from 22 WT and 22 shootin1 KO mice (15 mothers) and then transplanted into WT brains (n: 91 WT cells and 70 shootin1 KO cells counted from 6 WT brains). Two-tailed unpaired Student's t test, $p = 0.00435$, $t_{(159)} = 2.89$.

Data represent means ± SEM. *$p < 0.05$; **$p < 0.02$; ***$p < 0.01$. Scale bars: 400 μm for (A) and 100 μm for (C).

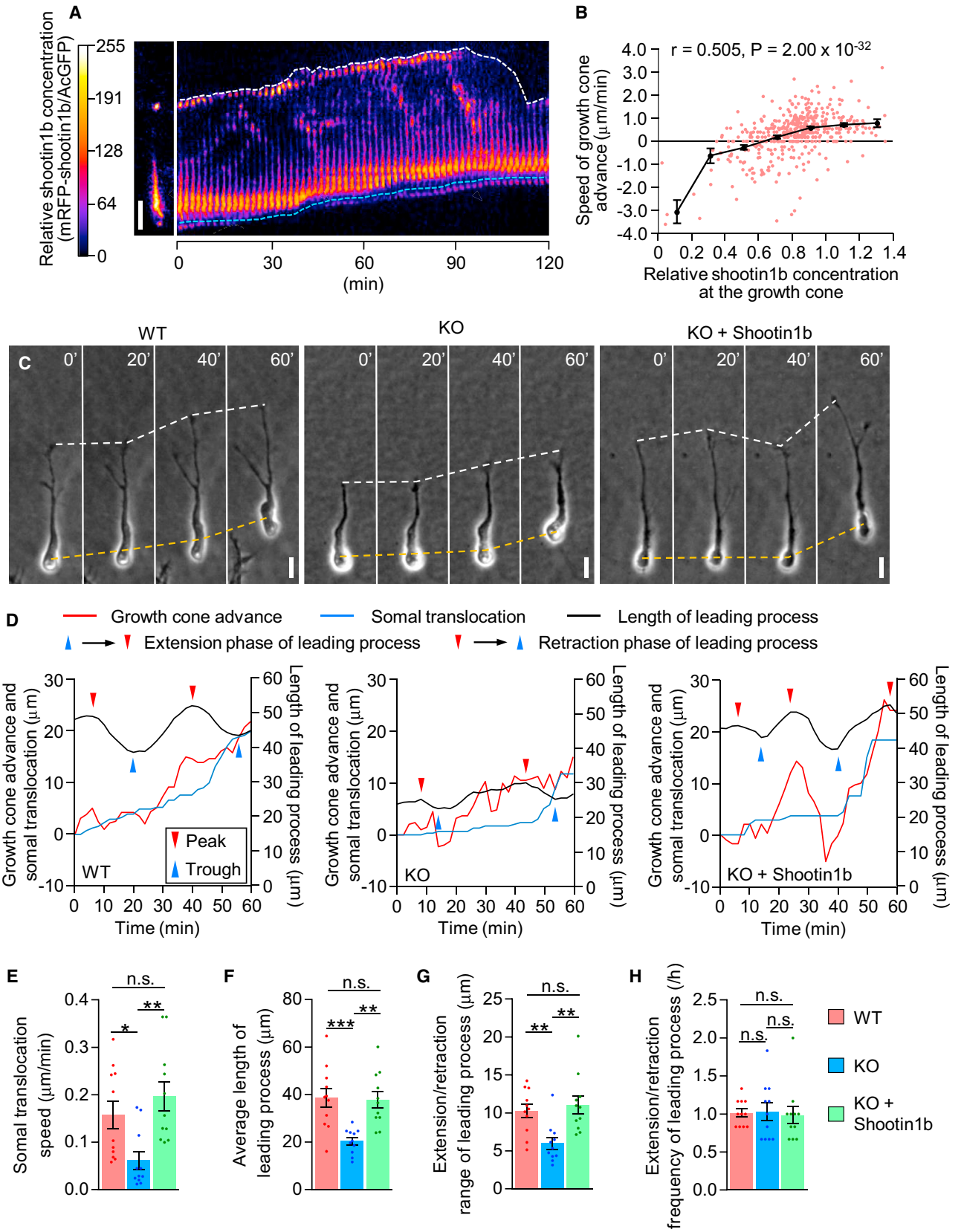

(legend on next page)

Together, these results suggest that shootin1b mediates leading process extension and somal translocation of olfactory interneurons.

As previous studies have reported that coupling between the centrosome and the nucleus plays a key role in somal translocation (Marín et al., 2010; Cooper, 2013; Kaneko et al., 2017), we further analyzed the dynamics of the centrosome and nucleus using their marker proteins centrin2 (White et al., 2000) and H2B (Kanda et al., 1998), respectively (Figures S4A and S4B). As reported (Belvindrah et al., 2017), the distance between centrosome and nucleus changed dynamically (Figures S4A and S4B). The mean distance between centrosome and nucleus was 3.1 ± 0.6 μm in WT neuroblasts; it was not affected significantly by shootin1 KO (Figure S4C). In addition, the range and frequency of the increase (blue arrowheads to red arrowheads, Figure S4B) and decrease (red arrowheads to blue arrowheads) of the centrosome-nucleus distance was not statistically different in WT and shootin1 KO neuroblasts (Figures S4D and S4E), thereby suggesting that shootin1 KO does not affect the centrosome-nucleus coupling.

Shootin1b Is Involved in the Generation of Traction Force at the Leading Process Growth Cone

To analyze the mechanics for the leading process extension and neuronal migration, we measured forces produced by migrating neuroblasts using traction force microscopy. P5 SVZ explants in a mixture of 75% Matrigel and 25% L-15 medium were plated on L1-CAM-Fc-coated acrylamide gels with embedded 200-nm fluorescent beads. Forces under the neuroblasts migrating from the explants in the semi-3D condition were monitored by visualizing force-induced deformation of the elastic substrate (Figure 5A), which is reflected by displacement of the beads from their original positions (Toriyama et al., 2013). Figure 5B and Video S4 show representative force mapping under a migrating WT neuroblast. Notably, prominent traction forces were observed under the growth cone of the leading processes (arrows 1, bead 5, Figure 5B), as reported in cerebellar granule cells (Jiang et al., 2015). The shaft of the leading processes did not produce remarkable forces. However, we noted intermittent appearance of actin wave-like structures bearing filopodia and lamellipodia (Ruthel and Banker, 1998; Inagaki and Katsuno, 2017) along the shaft (arrowheads, Figure S5); these structures produced traction forces (arrows, Figure S5), as reported in axonal actin waves (Katsuno et al., 2015). Cell bodies induced centripetal deformation of the substrate (arrows 2, Figure 5B), probably because of their weight. The direction of the deformation in front of the cell body changed from rearward to forward at the somal translocation step (pink arrows, bead 6, Figure 5B). We also noted centripetal traction forces under the tip of the trailing process (arrows 3, Figure 5B). As shootin1b accumulates at the leading process growth cone (Figures 2D–2F), we quantified the traction forces under the growth cones: the average net force produced by the growth cone was 9.7 ± 1.8 pN/μm^2 (n = 13 cells) and oriented toward the rear of the cell (Figures 5C and 5D; Video S5). The magnitude of the traction forces at the growth cone correlated positively with growth cone advance (Figure 5E, n = 13 cells), suggesting that the forces drive growth cone advance. In addition, the magnitude of the force was significantly reduced in shootin1 KO neuroblasts (4.53 ± 0.66 pN/μm^2, n = 11 cells, $p < 0.02$) (Figures 5C and 5D; Video S5). These results suggest that shootin1b is involved in the generation of traction force at the growth cone for leading process advance.

Shootin1b Mediates Clutch Coupling at the Leading Process Growth Cone

Next, we analyzed how shootin1b is involved in the force generation and leading process extension. As shown in Figures 6A–6C, shootin1b colocalized with F-actins, cortactin, and L1-CAM at the growth cones of the leading processes (arrowheads). We previously reported that shootin1a interacts with F-actin retrograde flow, through its interaction with cortactin, and with L1-CAM at axonal growth cones as a clutch molecule (Shimada et al., 2008; Kubo et al., 2015; Baba et al., 2018). These interactions, in turn, mechanically couple the F-actin flow with the adhesive substrates and thereby generate traction force for axon outgrowth (Kubo et al., 2015) and guidance (Abe et al., 2018; Baba et al., 2018). The regions of shootin1a that interact with cortactin (Kubo et al., 2015) and L1-CAM (Baba et al., 2018) are also present in shootin1b (Higashiguchi et al., 2016) (Figure S1).

To analyze whether shootin1b functions as a clutch molecule at the leading process growth cone, we performed fluorescent

Figure 4. Shootin1b Mediates Leading Process Extension and Somal Translocation of Olfactory Interneurons

(A) Shootin1b accumulation in a migrating neuroblast cultured in Matrigel. A fluorescence image of a neuroblast expressing mRFP-shootin1b and AcGFP were acquired every 2 min. The relative shootin1b concentration was calculated using AcGFP as an internal standard (mRFP-shootin1b/AcGFP) and is displayed by pseudocolor (see Video S2). A kymograph is shown on the right. White and blue dashed lines in the kymograph indicate the growth cone and soma, respectively.

(B) Speeds of growth cone advance plotted against relative shootin1b concentrations at growth cones (red dots). Speeds of growth cone advance were averaged in every 0.2 fraction of relative shootin1b concentrations and are shown as black dots with SEM (n = 480 from 8 cells). Pearson's correlation coefficient was calculated to determine the relationship between speed of growth cone advance and relative shootin1b concentration at the growth cone. r = 0.505, $p = 2.00 \times 10^{-32}$, $t_{(478)} = 12.8$.

(C) Phase-contrast time-lapse imaging of migrating WT (left) and shootin1 KO (middle and right) neuroblasts expressing AcGFP in Matrigel (see Video S3). KO neuroblasts were also transfected with FLAG-shootin1b expression vector (right). Images were acquired every 2 min. White and yellow dashed lines indicate the growth cone and soma, respectively.

(D) Growth cone advance (red lines), somal translocation (blue lines), and leading process length (black lines) monitored from WT and shootin1 KO neuroblasts in (C). Red and blue arrowheads indicate the peaks and troughs of the leading process length, respectively.

(E–H) Somal translocation speed (E) and average length (F), extension/retraction range (G), and extension/retraction frequency (H) of the leading process of WT and shootin1 KO neuroblasts. One-way ANOVA followed by Tukey's multiple comparisons test (n: 11 WT cells; 11 shoootin1 KO cells; 11 shootin1 KO cells expressing FLAG-shootin1b).

Data represent means ± SEM. *$p < 0.05$; **$p < 0.02$; ***$p < 0.01$; n.s., no significant difference. Scale bars: 20 μm for (A) and 10 μm for (C). See also Figure S4.

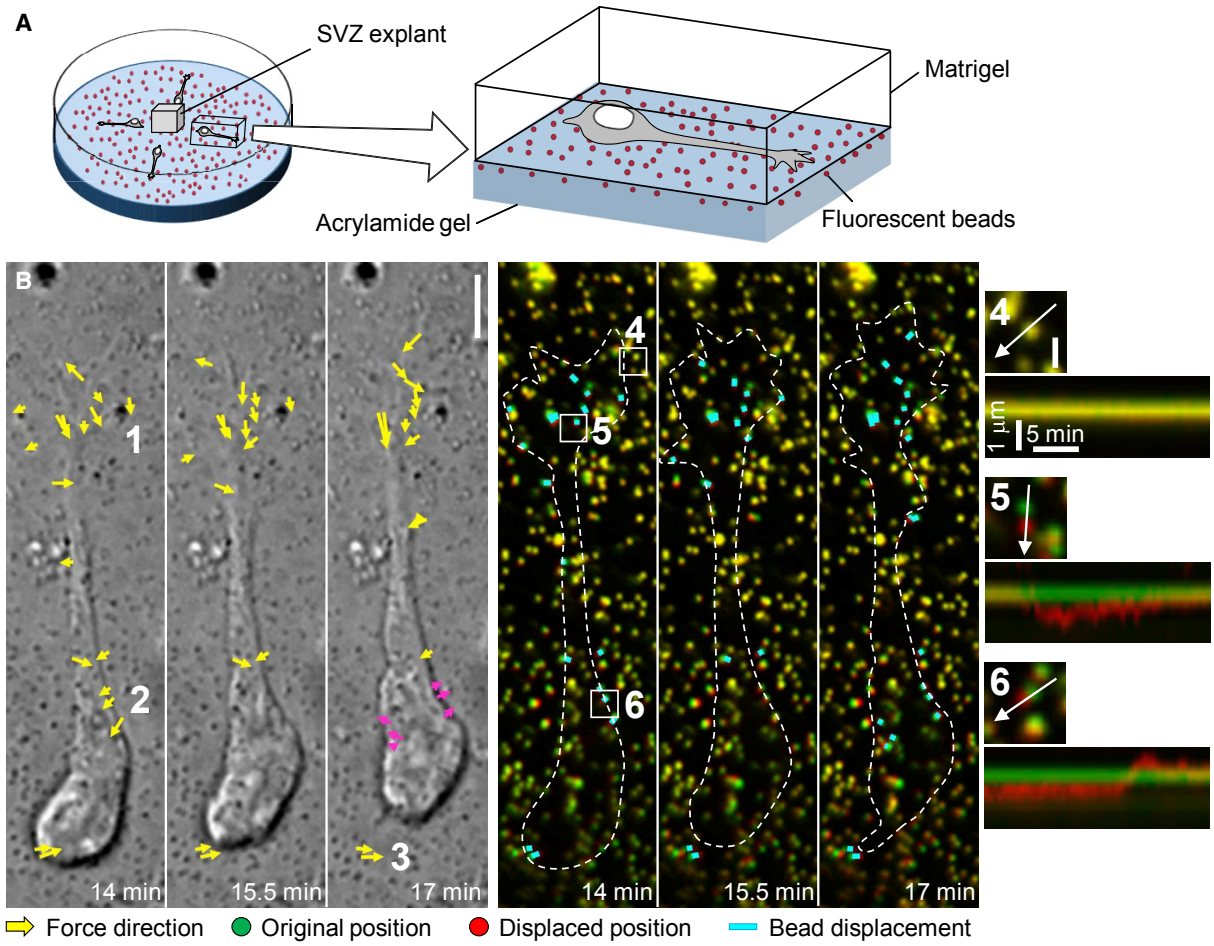

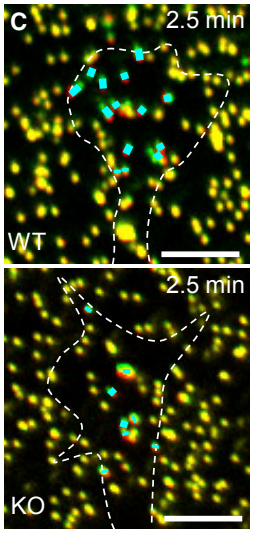

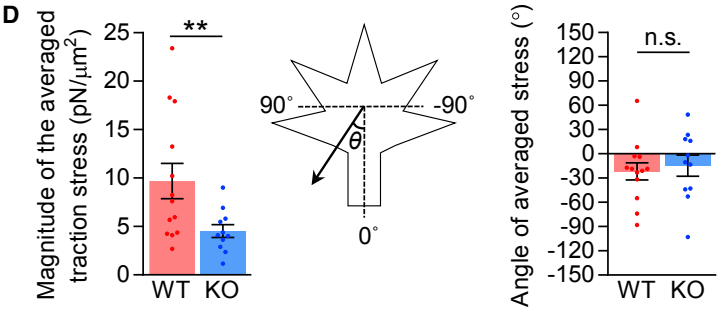

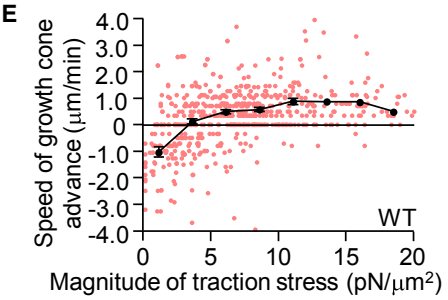

(legend on next page)

speckle imaging analysis (Watanabe and Mitchison, 2002; Shimada et al., 2008) of HaloTag-actin, HaloTag-shootin1b and HaloTag-cortactin expressed in neurons. Speckles of HaloTag-actin underwent retrograde flow at the leading process growth cone (Figure 6D; Video S6), as reported in the leading process growth cone of migratory cerebellar granule cells (He et al., 2010). HaloTag-shootin1b and HaloTag-cortactin also underwent similar retrograde movement (Figures 6E and 6F; Video S6), suggesting that shootin1b interacts with F-actin retrograde flow via cortactin. To determine whether shootin1b interacts with cortactin and L1-CAM, we performed co-immunoprecipitation assays using brain lysate and confirmed that shootin1b interacts with both cortactin and L1-CAM (Figures 6G and 6H). Their direct interactions were also demonstrated by *in vitro* binding assays with purified proteins (Figures S6A and S6B). Previous studies reported that disruption of clutch coupling increases the speed of F-actin flow (Suter et al., 1998; Toriyama et al., 2013); as expected, shootin1 KO increased significantly the F-actin flow rate at the leading process growth cone (Figure 6I; Video S7). Together, these results suggest that shootin1b couples F-actin retrograde flow and adhesive substrates at the tip of the leading process by interacting with cortactin and L1-CAM, as a clutch molecule.

Shootin1b-Mediated Clutch Coupling Is Required for Leading Process Extension and Migration of Olfactory Interneurons

Finally, we investigated whether the shootin1b-mediated F-actin-adhesion coupling promotes leading process dynamics and migration of olfactory interneurons. To do so, we disrupted the coupling by overexpressing a shootin1 dominant-negative (DN) mutant. A previous study reported that NES-shootin1 (261–377), which contains the amino acid residues 261–377 of shootin1a/shootin1b, acts as a DN mutant that disrupts the interaction between shootin1a and cortactin (Kubo et al., 2015). Consistent with that finding, the shootin1 DN overexpressed in HEK293T cells bound to cortactin and inhibited the interaction between shootin1b and cortactin (Figure S7A). Shootin1 DN overexpressed in the olfactory interneurons accumulated at the leading process growth cone (arrowheads, Figure S7B) and inhibited the accumulation of endogenous shootin1b at the growth cone (Figure S7C). Overexpression of shootin1 DN also led to significant increase in the F-actin flow rate at the growth cone on L1-CAM and laminin (Figures 7A and 7B). These data indicate that the DN mutant disrupts the clutch coupling mediated by shootin1b. As in the case of shootin1 KO (Figures 4C–4F), disruption of F-actin-adhesion coupling by overexpression of shootin1 DN reduced significantly the migration speed and leading process length of the interneurons (Figures 7C–7E). Shootin1 DN overexpression also inhibited the range of extension and retraction of leading processes (Figure 7F) but did not affect the frequency of their extension and retraction (Figure 7G). Taken together, these data demonstrate that shootin1b-mediated clutch coupling at the leading process growth cone drives the leading process extension and migration of olfactory interneurons.

DISCUSSION

In this study, we showed that shootin1b is expressed in migrating mouse olfactory interneurons and accumulates at their leading process growth cones. We demonstrated that shootin1b mechanically couples F-actin retrograde flow and cell adhesions, through its interactions with cortactin and L1-CAM, thereby generating traction force at the growth cone (Figure 7H). Loss of shootin1b inhibited leading process extension and tangential migration of olfactory interneurons. Furthermore, shootin1 KO reduced the number of cells in the distal RMS. These results demonstrate that shootin1b functions as a clutch molecule responsible for the migration of olfactory interneurons in the brain. In addition, our data provide evidence that neuronal cell migration and axon guidance can share similar molecular mechanics.

Molecular Mechanics of Shootin1b-Mediated Neuronal Migration

Cells undergo directional migration through force-based interactions with components of their extracellular environment including adhesive substrates and neighboring cells. Our force-mapping analyses revealed prominent traction forces under the leading process growth cone of migrating olfactory interneurons (Figure 5B). Traction forces under the leading process growth cone have also been reported in cerebellar granular cells (Jiang et al., 2015). The direction of the forces was oriented toward the rear of the cells (Figure 5D), and their magnitude showed a positive correlation with growth cone advance (Figure 5E), suggesting that driving force for the growth cone advance (rightmost black arrow, Figure 7H) is produced as a counterforce to the traction forces exerted on the substrate (yellow arrows). In addition, shootin1b accumulates to high levels at the growth cones, and shootin1 KO led to the reduction of the traction forces and concurrent inhibition of leading process extension and cell migration. Neuronal environments in the brain include laminin located on the extracellular matrix and L1-CAM presented on

Figure 5. Analysis of Traction Forces under Migrating Neuroblasts

(A) Schema of traction force microscopy in a semi-3D condition. SVZ explants prepared from P5 mice were placed on L1-CAM-coated polyacrylamide gel and covered with Matrigel. Traction forces under neuroblasts that migrated out from the SVZ explants were measured.

(B and C) Force mapping of WT and shootin1 KO neuroblasts. Differential interference contrast (DIC, B, left) and fluorescence (B, right, and C) time-lapse images of migrating neuroblasts (see Videos S4 and S5). Images were acquired every 30 s. The original and displaced positions of the beads are indicated by green and red, respectively, while the bead displacements are indicated by cyan lines. Arrows in DIC images indicate the magnitude and direction of traction forces (force magnitudes are shown by the length of arrows, which are 3 times longer than bead displacements). Dashed lines indicate the boundary of the cells.

(D) Statistical analysis of magnitude and angle (θ) of the traction forces under the growth cone of WT and shootin1 KO neuroblasts. Two-tailed unpaired Welch's t test, $p = 0.0176$, $t_{(15)} = 2.66$ (magnitude); two-tailed unpaired Student's t test, $p = 0.684$, $t_{(22)} = 0.412$ (angle) (n: 13 WT cells; 11 shoootin1 KO cells).

(E) Speed of the advance of WT growth cones were plotted against the magnitude of traction stresses under growth cones. The speeds of growth cone advance were averaged in every 2.5-pN/mm^2 fraction of the traction stress and are shown as black dots with SEM (n = 13 cells).

Data represent means ± SEM. **$p < 0.02$. n.s., no significant difference. Scale bars, 5 μm. See also Figure S5.

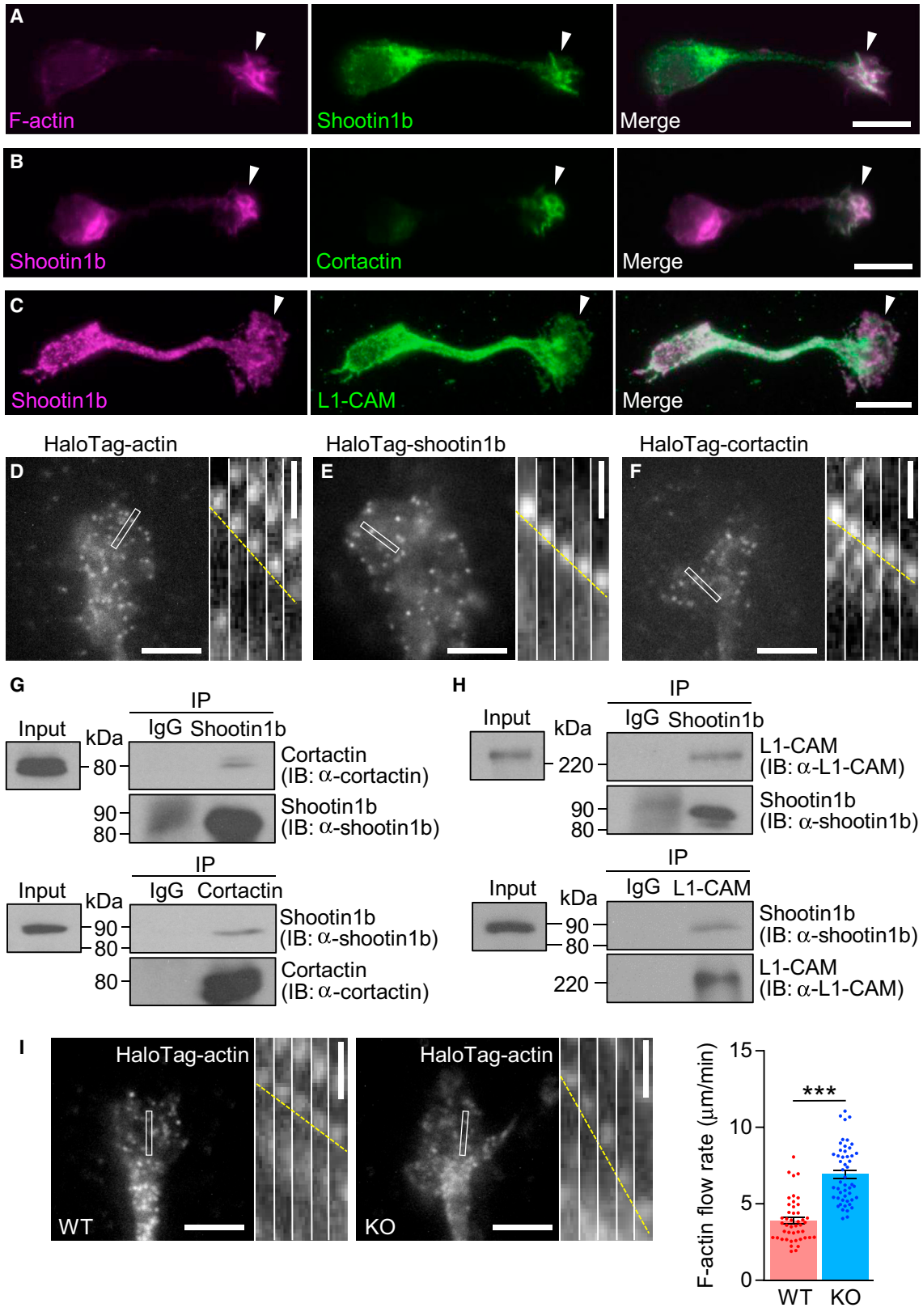

(legend on next page)

the neighboring cells (Mercurio, 1990; Kamiguchi et al., 1998). In this study, neurons were cultured on laminin-coated or L1-CAM-coated coverslips. In migration assays, they were cultured in Matrigel, which contains laminin. As L1-CAM on growth cones interacts with both laminin and L1-CAM presented on the substrate (Grumet et al., 1993; Hall et al., 1997; Abe et al., 2018), shootin1b and L1-CAM in the leading process growth cone can mediate the mechanical coupling between F-actin retrograde flow and both of the substrates. Together, these data suggest that the traction force generated by shootin1b-mediated clutch coupling at the growth cone plays a central role in shootin1b-induced migration of olfactory interneurons (Figure 7H).

We also observed centripetal deformation of the adhesive substrate around the soma. As the direction of the deformation in front of the soma changed from rearward to forward in the somal translocation step (pink arrows, bead 6, Figure 5B), we consider that the leading process pulls the soma in this step. Consistent with this notion, a previous report demonstrated that severing the leading process of cerebellar granule cells stopped the somal translocation (He et al., 2010). Shootin1b probably does not pull the soma directly, as it does not accumulate in front of the soma and its KO did not affect the centrosome-nucleus dynamics. We propose that shootin1b promotes the somal translocation step indirectly by increasing the tension of the leading process through shootin1b-mediated traction force at the growth cone (Figure 7H).

Shootin1 in the Formation and Growth of the Olfactory Bulb

The present study demonstrated that shootin1 is required for the formation and growth of the olfactory bulb. Thirty-five percent of shootin1 KO mice displayed agenesis of the olfactory bulb at birth, as a severe phenotype. The other 65% appeared to show normal morphology of the olfactory bulb on P0; however, 20% of them showed a reduction in olfactory bulb size on P5, as a mild phenotype. The impaired tangential migration of the shootin1 KO neuroblasts is consistent with the reduced number of cells in the distal RMS and the reduced growth of the olfactory bulb in the shootin1 KO mice with the mild phenotype. Similarly, double KO of mDia1 and mDia3 in mice is reported to result in both impaired tangential migration of neuroblasts and reduced size of the olfactory bulb (Shinohara et al., 2012). However, the agenesis of the olfactory bulb may not be attributable solely to the impaired migration of neuroblasts. For the formation of the olfactory bulb both radial migration of the excitatory projection neurons and tangential migration of the neuroblast play key roles (Hinds, 1968; Marín and Rubenstein, 2001; Blanchart et al., 2006; Ayala et al., 2007; Lledo et al., 2008). Interestingly, in the KO brains with the severe phenotype, the projection neurons assembled ectopically at the ventral forebrain region and did not form a typical mitral cell layer. Thus, these results suggest that the dysregulated migrations of the projection neurons and neuroblasts in shootin1 KO mice cooperatively result in the agenesis of the olfactory bulb. In this study, we also observed shootin1 KO mice with an apparently normal olfactory bulb. We consider that unknown molecules may functionally compensate for the loss of shootin1, in these mice, to ensure robust formation of the olfactory bulb.

Possible Involvement of Shootin1b in Neuronal Migration Guided by Extracellular Signals

Neuronal migration in the brain is regulated by diffusible and adhesive chemical signals (Marín et al., 2010; Sekine et al., 2012; Cooper, 2013; Evsyukova et al., 2013; Kaneko et al., 2017); the leading process growth cone is thought to sense these cues for directional migration (Cooper, 2013). Recent studies reported that the attractive axon guidance cue netrin-1 induces Pak1-mediated shootin1a phosphorylation via activation of Cdc42 and Rac1 (Toriyama et al., 2013; Kubo et al., 2015). The shootin1a phosphorylation in turn enhances shootin1a-mediated clutch coupling and thereby promotes traction force for the directional migration of axonal growth cones (Toriyama et al., 2013; Kubo et al., 2015; Baba et al., 2018). The clutch machinery involving shootin1a and L1-CAM also regulates axonal haptotaxis induced by substrate-bound laminin (Abe et al., 2018). Our present identification of shootin1b as a clutch molecule for neuronal migration raises the possibility that the regulation of neuronal migration by extracellular guidance cues is also mediated by clutch machinery. In addition, molecular clutch is proposed to explain mechanosensing during axon outgrowth and cell migration (Chan and Odde, 2008; Elosegui-Artola et al., 2018). Possible regulation of neuronal migration by their microenvironment through clutch machinery remains an important issue for future analyses.

STAR★METHODS

Detailed methods are provided in the online version of this paper and include the following:

- KEY RESOURCES TABLE
- CONTACT FOR REAGENT AND RESOURCE SHARING

Figure 6. Shootin1b Interacts with F-Actin Retrograde Flow and L1-CAM at the Leading Process Growth Cone

(A–C) DIV2 neuroblasts on laminin-coated coverslips co-stained with anti-shootin1b antibody (A–C), phalloidin for F-actin (A), anti-cortactin antibody (B), and anti-L1-CAM antibody (C). Arrowheads indicate the leading process growth cones.

(D–F) Fluorescent speckle images of HaloTag-actin (D), HaloTag-shootin1b (E), and HaloTag-cortactin (F) at the leading process growth cones of neuroblasts on L1-CAM-coated coverslips and kymographs of the boxed areas at 3-s intervals (right) (see Video S6). Dashed lines indicate the retrograde flow of speckles.

(G and H) Co-immunoprecipitation of endogenous shootin1b with cortactin (G) and L1-CAM (H) from E19 rat brain lysates. The brain lysates were incubated with control IgG (G and H, top and bottom), anti-shootin1b antibody (G and H, top), anti-cortactin antibody (G, bottom), or anti-L1-CAM antibody (H, bottom). The immunoprecipitates were immunoblotted with anti-shootin1b (G and H), anti-cortactin (G), or anti-L1-CAM (H) antibody. See also Figure S6.

(I) Fluorescent speckle images of HaloTag-actin at the leading process growth cones of WT and shootin1 KO neuroblasts on L1-CAM-coated coverslips (see Video S7). Kymographs of the boxed area are shown to the right at 3-s intervals. Dashed lines indicate the retrograde flow of HaloTag-actin speckles. F-actin retrograde flow rate (right graph) was measured from the kymograph analysis (n: 45 speckles for WT; 50 speckles for shootin1 KO). Two-tailed unpaired Student's t test, $p = 7.03 \times 10^{-14}$, $t_{(93)} = -8.80$.

Data represent means ± SEM. ***$p < 0.01$. Scale bars: 10 μm for (A)–(C), 5 μm for (D)–(F) and (I, left), and 1 μm for (D)–(F) and (I, right).

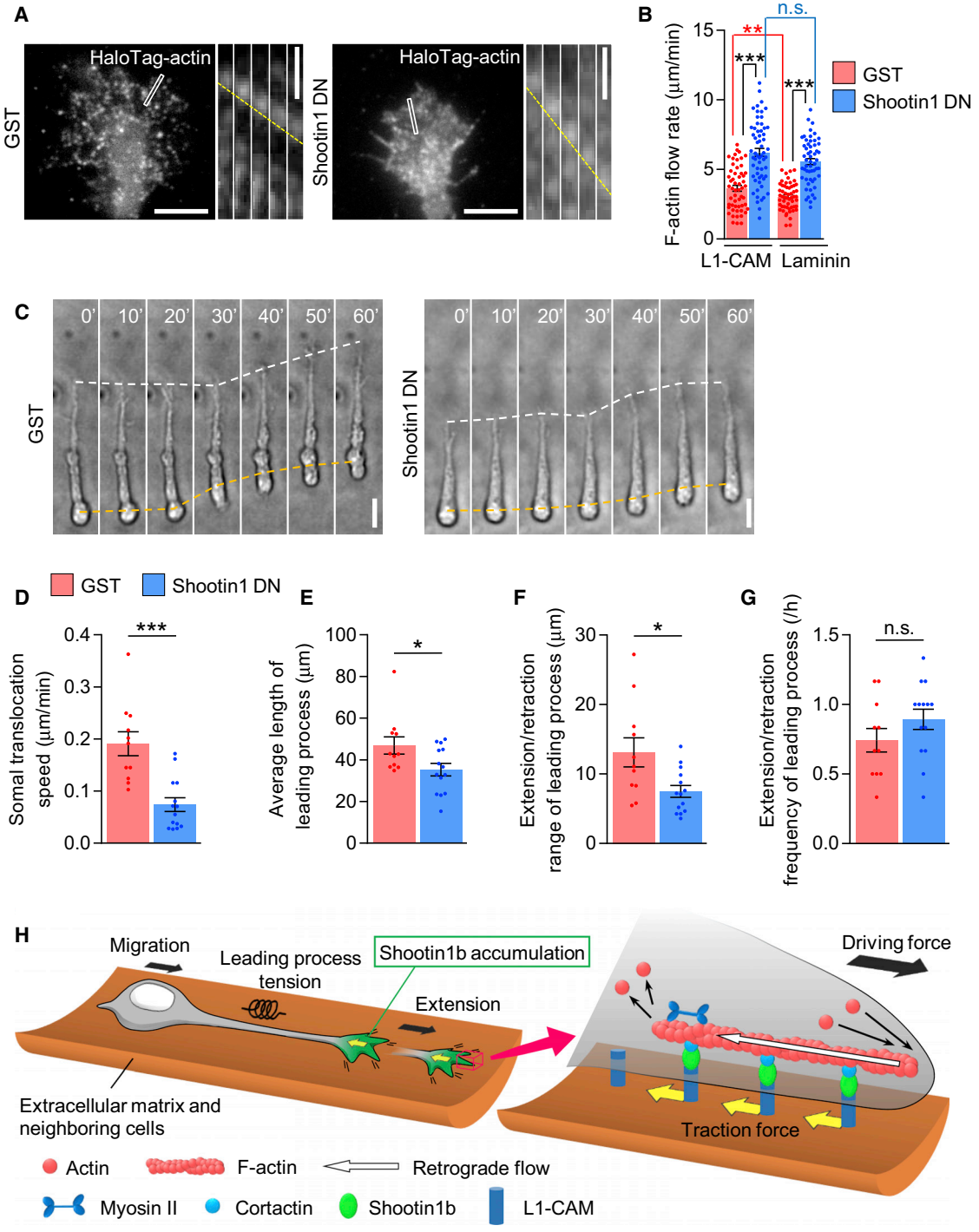

Figure 7. Shootin1b-Cortactin Coupling Is Required for Leading Process Extension and Migration of Olfactory Interneurons

(A) Fluorescent speckle images of HaloTag-actin at leading process growth cones of neuroblasts on L1-CAM-coated glass-bottom dishes overexpressing GST (control) or shootin1 DN. Kymographs of the boxed area are shown to the right at 3-s intervals. Dashed lines indicate the retrograde flow of HaloTag-actin speckles.

(B) F-actin retrograde flow rate was measured from the kymograph analysis in (A). Neurons were cultured on L1-CAM-coated or laminin-coated dishes. On L1-CAM-coated dishes, n = 55 speckles for GST and n = 60 speckles for shootin1 DN. On laminin-coated dishes, n = 55 speckles for GST and n = 55 speckles for shootin1 DN.

(legend continued on next page)

SUPPLEMENTAL INFORMATION

Supplemental Information includes seven figures, one table, and seven videos and can be found with this article online at https://doi.org/10.1016/j.celrep.2018.09.068.

ACKNOWLEDGMENTS

We thank Y. Sakumura, M. Toriyama, T. Hakoshima, and S. Suetsugu for discussions. This research was supported in part by AMED under grant number JP18gm0810011, a JSPS Grant-in-Aid for Scientific Research on Innovative Areas (JP25102010), JSPS KAKENHI (JP23370088 and JP26290007), the Osaka Medical Research Foundation for Incurable Diseases, and the Takeda Science Foundation.

AUTHOR CONTRIBUTIONS

T.M., Y.U., N.K., W.Y., K.S., and N.I. designed the experiments. T.M., Y.U., N.K., and W.Y. performed experiments and data analysis. T.M., N.K., and N.I. wrote the manuscript. N.I. supervised the project. All authors discussed the results and commented on the manuscript.

DECLARATION OF INTERESTS

The authors declare no competing interests.

Received: April 2, 2018
Revised: August 31, 2018
Accepted: September 21, 2018
Published: October 16, 2018

REFERENCES

Abe, K., Katsuno, H., Toriyama, M., Baba, K., Mori, T., Hakoshima, T., Kanemura, Y., Watanabe, R., and Inagaki, N. (2018). Grip and slip of L1-CAM on adhesive substrates direct growth cone haptotaxis. Proc. Natl. Acad. Sci. USA *115*, 2764–2769.

Ayala, R., Shu, T., and Tsai, L.H. (2007). Trekking across the brain: The journey of neuronal migration. Cell *128*, 29–43.

Baba, K., Yoshida, W., Toriyama, M., Shimada, T., Manning, C.F., Saito, M., Kohno, K., Trimmer, J.S., Watanabe, R., and Inagaki, N. (2018). Gradient-reading and mechano-effector machinery for netrin-1-induced axon guidance. eLife *7*, e34593.

Bard, L., Boscher, C., Lambert, M., Mège, R.M., Choquet, D., and Thoumine, O. (2008). A molecular clutch between the actin flow and N-cadherin adhesions drives growth cone migration. J. Neurosci. *28*, 5879–5890.

Bellion, A., Baudoin, J.P., Alvarez, C., Bornens, M., and Métin, C. (2005). Nucleokinesis in tangentially migrating neurons comprises two alternating phases: Forward migration of the Golgi/centrosome associated with centrosome splitting and myosin contraction at the rear. J. Neurosci. *25*, 5691–5699.

Belvindrah, R., Lazarini, F., and Lledo, P.M. (2009). Postnatal neurogenesis: From neuroblast migration to neuronal integration. Rev. Neurosci. *20*, 331–346.

Belvindrah, R., Natarajan, K., Shabajee, P., Bruel-Jungerman, E., Bernard, J., Goutierre, M., Moutkine, I., Jaglin, X.H., Savariradjane, M., Irinopoulou, T., et al. (2017). Mutation of the α-tubulin Tuba1a leads to straighter microtubules and perturbs neuronal migration. J. Cell Biol. *216*, 2443–2461.

Besse, L., Neti, M., Anselme, I., Gerhardt, C., Rüther, U., Laclef, C., and Schneider-Maunoury, S. (2011). Primary cilia control telencephalic patterning and morphogenesis via Gli3 proteolytic processing. Development *138*, 2079–2088.

Blanchart, A., De Carlos, J.A., and López-Mascaraque, L. (2006). Time frame of mitral cell development in the mice olfactory bulb. J. Comp. Neurol. *496*, 529–543.

Bulfone, A., Puelles, L., Porteus, M.H., Frohman, M.A., Martin, G.R., and Rubenstein, J.L. (1993). Spatially restricted expression of Dlx-1, Dlx-2 (Tes-1), Gbx-2, and Wnt-3 in the embryonic day 12.5 mouse forebrain defines potential transverse and longitudinal segmental boundaries. J. Neurosci. *13*, 3155–3172.

Chan, C.E., and Odde, D.J. (2008). Traction dynamics of filopodia on compliant substrates. Science *322*, 1687–1691.

Charras, G., and Sahai, E. (2014). Physical influences of the extracellular environment on cell migration. Nat. Rev. Mol. Cell Biol. *15*, 813–824.

Cooper, J.A. (2013). Cell biology in neuroscience: Mechanisms of cell migration in the nervous system. J. Cell Biol. *202*, 725–734.

(C) Phase-contrast time-lapse imaging of neuroblasts in Matrigel overexpressing GST or shootin1 DN. Images were acquired every 2 min. White and yellow dashed lines indicate the growth cone and soma, respectively.
(D–G) Somal translocation speed (D) and average length (E), extension/retraction range (F), and extension/retraction frequency (G) of the leading process of neuroblasts overexpressing GST or shootin1 DN. Two-tailed unpaired Student's t test: (D) p = 0.000117, $t_{(23)}$ = 4.63; (E) p = 0.0288, $t_{(23)}$ = 2.33. Two-tailed unpaired Welch's t test: (F) p = 0.0266, $t_{(13)}$ = 2.50; (G) p = 0.195, $t_{(21)}$ = −1.34. GST, n = 11 cells; shootin1 DN, n = 14 cells.
(H) A model for shootin1b-driven leading process extension and somal translocation. At the leading process growth cone, shootin1b mediates a mechanical clutch coupling between F-actin retrograde flow and cell adhesions, through its interactions with cortactin and L1-CAM. This coupling generates traction force under the growth cone (yellow arrows). The driving force for the growth cone advance (rightmost black arrow) is produced as a counterforce to the traction forces exerted on the adhesive substrate (yellow arrows). In addition, shootin1b may promote somal translocation by increasing indirectly the tension of the leading process, which pulls the soma forward.
Data represent means ± SEM. *p < 0.05; ***p < 0.01; n.s., no significant difference. Scale bars: 5 μm for (A, left), 1 μm for (A, right), and 10 μm for (C). See also Figure S7.

Elosegui-Artola, A., Trepat, X., and Roca-Cusachs, P. (2018). Control of mechanotransduction by molecular clutch dynamics. Trends Cell Biol. *28*, 356–367.

Evsyukova, I., Plestant, C., and Anton, E.S. (2013). Integrative mechanisms of oriented neuronal migration in the developing brain. Annu. Rev. Cell Dev. Biol. *29*, 299–353.

Garcia, M., Leduc, C., Lagardère, M., Argento, A., Sibarita, J.B., and Thoumine, O. (2015). Two-tiered coupling between flowing actin and immobilized N-cadherin/catenin complexes in neuronal growth cones. Proc. Natl. Acad. Sci. USA *112*, 6997–7002.

Gardel, M.L., Schneider, I.C., Aratyn-Schaus, Y., and Waterman, C.M. (2010). Mechanical integration of actin and adhesion dynamics in cell migration. Annu. Rev. Cell Dev. Biol. *26*, 315–333.

Ghashghaei, H.T., Lai, C., and Anton, E.S. (2007). Neuronal migration in the adult brain: Are we there yet? Nat. Rev. Neurosci. *8*, 141–151.

Grumet, M., Friedlander, D.R., and Edelman, G.M. (1993). Evidence for the binding of Ng-CAM to laminin. Cell Adhes. Commun. *1*, 177–190.

Hall, H., Carbonetto, S., and Schachner, M. (1997). L1/HNK-1 carbohydrate- and beta 1 integrin-dependent neural cell adhesion to laminin-1. J. Neurochem. *68*, 544–553.

He, M., Zhang, Z.H., Guan, C.B., Xia, D., and Yuan, X.B. (2010). Leading tip drives soma translocation via forward F-actin flow during neuronal migration. J. Neurosci. *30*, 10885–10898.

Higashiguchi, Y., Katsuta, K., Minegishi, T., Yonemura, S., Urasaki, A., and Inagaki, N. (2016). Identification of a shootin1 isoform expressed in peripheral tissues. Cell Tissue Res. *366*, 75–87.

Hinds, J.W. (1968). Autoradiographic study of histogenesis in the mouse olfactory bulb. II. Cell proliferation and migration. J. Comp. Neurol. *134*, 305–322.

Inagaki, N., and Katsuno, H. (2017). Actin waves: Origin of cell polarization and migration? Trends Cell Biol. *27*, 515–526.

Jiang, J., Zhang, Z.H., Yuan, X.B., and Poo, M.M. (2015). Spatiotemporal dynamics of traction forces show three contraction centers in migratory neurons. J. Cell Biol. *209*, 759–774.

Kamiguchi, H., Hlavin, M.L., Yamasaki, M., and Lemmon, V. (1998). Adhesion molecules and inherited diseases of the human nervous system. Annu. Rev. Neurosci. *21*, 97–125.

Kanda, T., Sullivan, K.F., and Wahl, G.M. (1998). Histone-GFP fusion protein enables sensitive analysis of chromosome dynamics in living mammalian cells. Curr. Biol. *8*, 377–385.

Kaneko, N., Marín, O., Koike, M., Hirota, Y., Uchiyama, Y., Wu, J.Y., Lu, Q., Tessier-Lavigne, M., Alvarez-Buylla, A., Okano, H., et al. (2010). New neurons clear the path of astrocytic processes for their rapid migration in the adult brain. Neuron *67*, 213–223.

Kaneko, N., Sawada, M., and Sawamoto, K. (2017). Mechanisms of neuronal migration in the adult brain. J. Neurochem. *141*, 835–847.

Katsuno, H., Toriyama, M., Hosokawa, Y., Mizuno, K., Ikeda, K., Sakumura, Y., and Inagaki, N. (2015). Actin migration driven by directional assembly and disassembly of membrane-anchored actin filaments. Cell Rep. *12*, 648–660.

Kubo, Y., Baba, K., Toriyama, M., Minegishi, T., Sugiura, T., Kozawa, S., Ikeda, K., and Inagaki, N. (2015). Shootin1-cortactin interaction mediates signal-force transduction for axon outgrowth. J. Cell Biol. *210*, 663–676.

Lämmermann, T., Bader, B.L., Monkley, S.J., Worbs, T., Wedlich-Söldner, R., Hirsch, K., Keller, M., Förster, R., Critchley, D.R., Fässler, R., and Sixt, M. (2008). Rapid leukocyte migration by integrin-independent flowing and squeezing. Nature *453*, 51–55.

Lim, D.A., and Alvarez-Buylla, A. (2016). The adult ventricular-subventricular zone (V-SVZ) and olfactory bulb (OB) neurogenesis. Cold Spring Harb. Perspect. Biol. *8*, a018820.

Lledo, P.M., Merkle, F.T., and Alvarez-Buylla, A. (2008). Origin and function of olfactory bulb interneuron diversity. Trends Neurosci. *31*, 392–400.

Lowery, L.A., and Van Vactor, D. (2009). The trip of the tip: Understanding the growth cone machinery. Nat. Rev. Mol. Cell Biol. *10*, 332–343.

Marín, O., and Rubenstein, J.L. (2001). A long, remarkable journey: Tangential migration in the telencephalon. Nat. Rev. Neurosci. *2*, 780–790.

Marín, O., and Rubenstein, J.L.R. (2003). Cell migration in the forebrain. Annu. Rev. Neurosci. *26*, 441–483.

Marín, O., Valiente, M., Ge, X., and Tsai, L.H. (2010). Guiding neuronal cell migrations. Cold Spring Harb. Perspect. Biol. *2*, a001834.

Martini, F.J., and Valdeolmillos, M. (2010). Actomyosin contraction at the cell rear drives nuclear translocation in migrating cortical interneurons. J. Neurosci. *30*, 8660–8670.

Medeiros, N.A., Burnette, D.T., and Forscher, P. (2006). Myosin II functions in actin-bundle turnover in neuronal growth cones. Nat. Cell Biol. *8*, 215–226.

Mercurio, A.M. (1990). Laminin: Multiple forms, multiple receptors. Curr. Opin. Cell Biol. *2*, 845–849.

Mitchison, T., and Kirschner, M. (1988). Cytoskeletal dynamics and nerve growth. Neuron *1*, 761–772.

Ota, H., Hikita, T., Sawada, M., Nishioka, T., Matsumoto, M., Komura, M., Ohno, A., Kamiya, Y., Miyamoto, T., Asai, N., et al. (2014). Speed control for neuronal migration in the postnatal brain by Gmip-mediated local inactivation of RhoA. Nat. Commun. *5*, 4532.

Petrie, R.J., Koo, H., and Yamada, K.M. (2014). Generation of compartmentalized pressure by a nuclear piston governs cell motility in a 3D matrix. Science *345*, 1062–1065.

Pollard, T.D., and Borisy, G.G. (2003). Cellular motility driven by assembly and disassembly of actin filaments. Cell *112*, 453–465.

Rathjen, F.G., and Schachner, M. (1984). Immunocytological and biochemical characterization of a new neuronal cell surface component (L1 antigen) which is involved in cell adhesion. EMBO J. *3*, 1–10.

Rivas, R.J., and Hatten, M.E. (1995). Motility and cytoskeletal organization of migrating cerebellar granule neurons. J. Neurosci. *15*, 981–989.

Ruthel, G., and Banker, G. (1998). Actin-dependent anterograde movement of growth-cone-like structures along growing hippocampal axons: A novel form of axonal transport? Cell Motil. Cytoskeleton *40*, 160–173.

Schaar, B.T., and McConnell, S.K. (2005). Cytoskeletal coordination during neuronal migration. Proc. Natl. Acad. Sci. USA *102*, 13652–13657.

Sekine, K., Kawauchi, T., Kubo, K., Honda, T., Herz, J., Hattori, M., Kinashi, T., and Nakajima, K. (2012). Reelin controls neuronal positioning by promoting cell-matrix adhesion via inside-out activation of integrin $\alpha5\beta1$. Neuron *76*, 353–369.

Shimada, T., Toriyama, M., Uemura, K., Kamiguchi, H., Sugiura, T., Watanabe, N., and Inagaki, N. (2008). Shootin1 interacts with actin retrograde flow and L1-CAM to promote axon outgrowth. J. Cell Biol. *181*, 817–829.

Shinohara, R., Thumkeo, D., Kamijo, H., Kaneko, N., Sawamoto, K., Watanabe, K., Takebayashi, H., Kiyonari, H., Ishizaki, T., Furuyashiki, T., and Narumiya, S. (2012). A role for mDia, a Rho-regulated actin nucleator, in tangential migration of interneuron precursors. Nat. Neurosci. *15*, 373–380, S1–S2.

Shu, T., Ayala, R., Nguyen, M.D., Xie, Z., Gleeson, J.G., and Tsai, L.H. (2004). Ndel1 operates in a common pathway with LIS1 and cytoplasmic dynein to regulate cortical neuronal positioning. Neuron *44*, 263–277.

Solecki, D.J. (2012). Sticky situations: Recent advances in control of cell adhesion during neuronal migration. Curr. Opin. Neurobiol. *22*, 791–798.

Stroka, K.M., Jiang, H., Chen, S.H., Tong, Z., Wirtz, D., Sun, S.X., and Konstantopoulos, K. (2014). Water permeation drives tumor cell migration in confined microenvironments. Cell *157*, 611–623.

Suter, D.M., and Forscher, P. (2000). Substrate-cytoskeletal coupling as a mechanism for the regulation of growth cone motility and guidance. J. Neurobiol. *44*, 97–113.

Suter, D.M., Errante, L.D., Belotserkovsky, V., and Forscher, P. (1998). The Ig superfamily cell adhesion molecule, apCAM, mediates growth cone steering by substrate-cytoskeletal coupling. J. Cell Biol. *141*, 227–240.

Tanaka, T., Serneo, F.F., Higgins, C., Gambello, M.J., Wynshaw-Boris, A., and Gleeson, J.G. (2004). Lis1 and doublecortin function with dynein to mediate

coupling of the nucleus to the centrosome in neuronal migration. J. Cell Biol. *165*, 709–721.

Toriyama, M., Shimada, T., Kim, K.B., Mitsuba, M., Nomura, E., Katsuta, K., Sakumura, Y., Roepstorff, P., and Inagaki, N. (2006). Shootin1: A protein involved in the organization of an asymmetric signal for neuronal polarization. J. Cell Biol. *175*, 147–157.

Toriyama, M., Kozawa, S., Sakumura, Y., and Inagaki, N. (2013). Conversion of a signal into forces for axon outgrowth through Pak1-mediated shootin1 phosphorylation. Curr. Biol. *23*, 529–534.

Tsai, L.H., and Gleeson, J.G. (2005). Nucleokinesis in neuronal migration. Neuron *46*, 383–388.

Tucker, E.S., Polleux, F., and LaMantia, A.S. (2006). Position and time specify the migration of a pioneering population of olfactory bulb interneurons. Dev. Biol. *297*, 387–401.

Watanabe, N., and Mitchison, T.J. (2002). Single-molecule speckle analysis of actin filament turnover in lamellipodia. Science *295*, 1083–1086.

Weed, S.A., and Parsons, J.T. (2001). Cortactin: Coupling membrane dynamics to cortical actin assembly. Oncogene *20*, 6418–6434.

White, R.A., Pan, Z., and Salisbury, J.L. (2000). GFP-centrin as a marker for centriole dynamics in living cells. Microsc. Res. Tech. *49*, 451–457.

Wichterle, H., Garcia-Verdugo, J.M., and Alvarez-Buylla, A. (1997). Direct evidence for homotypic, glia-independent neuronal migration. Neuron *18*, 779–791.

Young, K.M., Fogarty, M., Kessaris, N., and Richardson, W.D. (2007). Subventricular zone stem cells are heterogeneous with respect to their embryonic origins and neurogenic fates in the adult olfactory bulb. J. Neurosci. *27*, 8286–8296.

STAR★METHODS

KEY RESOURCES TABLE

REAGENT or RESOURCE	SOURCE	IDENTIFIER
Antibodies		
Rabbit polyclonal anti-shootin1	(Toriyama et al., 2006)	N/A
Rabbit polyclonal anti-shootin1a	(Baba et al., 2018)	N/A
Rabbit polyclonal anti-shootin1b	(Higashiguchi et al., 2016)	N/A
Rabbit polyclonal anti-Tbr2	Abcam	Cat# ab23345; RRID: AB_778267
Rabbit polyclonal anti-myc tag	MBL	Cat# 562S; RRID: AB_591114
Rabbit polyclonal anti-GFP	MBL	Cat# 598S; RRID: AB_591816
Mouse monoclonal anti-FLAG M2	Sigma	Cat# F3165; RRID: AB_259529
Goat polyclonal anti-doublecortin	Santa Cruz Biotechnology	Cat# sc-8066; RRID: AB_2088494
Goat polyclonal anti-L1	Santa Cruz Biotechnology	Cat# sc-1508; RRID: AB_631086
Mouse monoclonal anti-cortactin	Millipore	Cat# 05-180; RRID: AB_309647
Mouse monoclonal anti-actin	Millipore	Cat# MAB1501R; RRID: AB_2223041
Alexa 594 conjugated donkey anti-rabbit	Jackson ImmunoResearch Labs	Cat# 711-585-152; RRID: AB_ 2340621
Alexa 488 conjugated goat anti-rabbit	Thermo Fisher Scientific	Cat# A-11008; RRID: AB_143165
Alexa 488 conjugated goat anti-mouse	Thermo Fisher Scientific	Cat# A-11029; RRID: AB_2534088
Alexa 488 conjugated donkey anti-goat	Thermo Fisher Scientific	Cat# A-11055; RRID: AB_ 2534102
HRP conjugated donkey anti-rabbit	GE Healthcare	Cat# NA934; RRID: AB_772206
HRP conjugated goat anti-mouse	Thermo Fisher Scientific	Cat# AP308P; RRID: AB_92635
HRP conjugated donkey anti-goat	Millipore	Cat# AP180P; RRID: AB_92573
Rabbit control IgG	Sigma	Cat# I8140; RRID: AB_1163661
Mouse control IgG	Santa Cruz Biotechnology	Cat# sc-2025; RRID: AB_737182
Goat control IgG	Santa Cruz Biotechnology	Cat# sc-2028; RRID: AB_737167
Chemicals, Peptides, and Recombinant Proteins		
Alexa 594 phalloidin	Thermo Fisher Scientific	Cat# A12381
CMAC	Thermo Fisher Scientific	Cat# C2110
DAPI	Thermo Fisher Scientific	Cat# D1306
ProLong Gold	Thermo Fisher Scientific	Cat# P36930
PDL	Sigma	Cat# P6407-5MG
Laminin	Lonza	Cat# 120-05751
L1-CAM-Fc	(Shimada et al., 2008)	N/A
Matrigel	Corning	Cat# 356237
HaloTag TMR ligand	Promega	Cat# G8251
Critical Commercial Assays		
Protein G Sepharose 4 Fast Flow	GE Healthcare	Cat# 17061801
Anti-Myc tag mAb-Magnetic Beads	MBL	Cat# M047-11
FLAG-peptide	Sigma	Cat# F3290-4MG
Mouse Neuron Nucleofector Kit	Lonza	Cat# VPG-1001
PKH26 Red Fluorescent Cell Linker Kit	Sigma	Cat# PKH26GL
PKH67 Green Fluorescent Cell Linker Kit	Sigma	Cat# PKH67GL
Experimental Models: Organisms/Strains		
Mouse C57BL/6	Japan SLC; CLEA Japan	N/A
Mouse Shootin1 KO	(Baba et al., 2018)	N/A
Mouse ICR	Japan SLC	N/A
Rat Wistar	Japan SLC; CLEA Japan	N/A

(*Continued on next page*)

Continued

REAGENT or RESOURCE	SOURCE	IDENTIFIER
Oligonucleotides		
See Table S1 for oligonucleotide sequences	This study	N/A
Recombinant DNA		
pGEX-myc-shootin1b	This study	N/A
pmRFP-shootin1b	This study	N/A
pCMV-myc-shootin1b	This study	N/A
pCMV-FLAG-shootin1b	This study	N/A
pmRFP-H2B	This study	N/A
pmNeonGreen-centrin2	This study	N/A
pFN21A-HaloTag-actin	This study	N/A
pFN21A-HaloTag-cortactin	This study	N/A
pFN21A-HaloTag-shootin1b	This study	N/A
pCAGGS-NES-myc-GST	(Shimada et al., 2008)	N/A
pCAGGS-NES-myc-shootin1 (261-377)	(Kubo et al., 2015)	N/A
pCMV-FLAG-cortactin	(Kubo et al., 2015)	N/A
pCAGGS-EGFP-NES	This study	N/A
pCAGGS-EGFP-NES-shootin1 (261-377)	This study	N/A
Software and Algorithms		
ImageJ software	National Institutes of Health	https://imagej.nih.gov/ij/index.html; RRID: SCR_003070
MATLAB Version R2013b	Mathworks	https://www.mathworks.com; RRID: SCR_001622
Graph PadPrism7	GraphPad Software	https://www.graphpad.com/; RRID: SCR_002798
Axiovison3	Carl Zeiss	https://www.zeiss.com/microscopy/en_de/products/microscope-software/axiovision-for-biology.html; RRID: SCR_002677
ZEN software	Carl Zeiss	https://www.zeiss.com/microscopy/int/products/microscope-software/zen.html; RRID: SCR_013672
Metamorph	Molecular Devices	https://www.moleculardevices.com/products/cellular-imaging-systems/acquisition-and-analysis-software/metamorph-microscopy; RRID:SCR_002368

CONTACT FOR REAGENT AND RESOURCE SHARING

Further information and requests for reagents should be directed to and will be fulfilled by the Lead Contact, Naoyuki Inagaki (ninagai@bs.naist.jp).

MODEL SYSTEMS AND PERMISSIONS

All relevant aspects of the experimental procedures were approved by the Institutional Animal Care and Use Committee of Nara Institute of Science and Technology and Nagoya City University Graduate School of Medical Sciences. Embryonic stages were calculated from noon of the vaginal plug day, which was defined as embryonic day 0.5 (E0.5). E12.5, E14,5, E16.5, E18 C57BL/6 pregnant mice, P5 C57BL/6 mice, P7-8 ICR mice and E19 Wistar pregnant rats were obtained from Japan SLC and CLEA Japan. P2-5 shootin1 KO C57BL/6 mice and the littermates, P2-5 wild-type C57BL/6 mice, were obtained by housing with their mother under standard condition (12h/12h light/dark cycle, access to dry food and water). Mice and rats of both sexes in each developmental stage and in each age were used for experiments.

EXPERIMENTAL MODEL AND SUBJECT DETAILS

Animals

The generation of shootin1 KO mice is described elsewhere (Baba et al., 2018). Chimeric mice were crossed with C57BL/6 mice for at least seven generations before analysis. Male and female shootin1 heterozygous mice were mated to obtain shootin1 KO mice; the offspring genotypes were checked by PCR with the following primers: Genotyping F1 (5′-CAGACTGCTACCCACTACCCCCTAC-3′),

Genotyping R1 (5′-CCTAGAGCTGGACAGCGGATCTGAG-3′), Genotyping F2 (5′-CCCAGAAAGCGAAGGAACAAAGCTG-3′), and Genotyping R2 (5′-ACCTTGCTCCTTCAAGCTGGTGATG-3′). As described elsewhere (Baba et al., 2018), shootin1 KO mice also exhibit agenesis of the septum. For the analyses of neuronal migration in the RMS, we used neuroblasts prepared from shootin1 KO mice exhibiting abnormality in the OB or septum.

SVZ explant culture

Brains were taken from P5 mice and placed in ice-cold Leibovitz's L-15 medium (L-15, Thermo Fisher Scientific, USA). The SVZs were dissected from the brains and cut into blocks 100-150 μm in diameter, which were embedded in a mixture of 75% Matrigel (Corning) and 25% L-15 medium, and cultured in Neurobasal medium (Thermo Fisher Scientific) containing 2% B-27 supplement (Thermo Fisher Scientific), 1 mM glutamine (Nacalai Tesque) in a humidified, 5% CO_2, 37°C incubator.

Culture of dissociated cells and transfection

The SVZs dissected from P5 mouse brains were dissociated with papain as described previously (Toriyama et al., 2006). The dissociated cells were cultured on coverslips (Matsunami) or glass bottom dishes (Matsunami) coated with laminin or L1-CAM-Fc as described (Toriyama et al., 2006; Shimada et al., 2008). Cells were transfected with vectors using Nucleofector (Lonza). For experiments in Figures 4, 7C, and S4A, transfected cells were re-aggregated in Neurobasal medium (Thermo Fisher Scientific) containing 10% fatal bovine serum (FBS, Japan Bio Serum), 2% B-27 supplement and 1 mM glutamine for 5-7 h. The aggregates were then embedded in a mixture of 75% Matrigel and 25% L-15 medium, and cultured as described above.

Culture and transfection of HEK293T cells

HEK293T cells (ATCC) were cultured in Dulbecco's modified Eagle's medium (Sigma) containing 10% FBS (Japan Bio Serum) as described previously (Baba et al., 2018), and transfected with vectors using Polyethylenimine MAX (PEI MAX, Polysciences) following the manufacture's protocol.

Transplantation of SVZ cells

For transplantation experiments, the SVZs obtained from P2-5 WT or shootin1 KO mice were dissected and dissociated using trypsin-EDTA (Invitrogen) as previously described (Kaneko et al., 2010). The dissociated cells were labeled using the PKH-26 or PKH-67 Fluorescent Cell Linker Kit (Sigma), and then resuspended in L-15 medium. The cell suspension (1.6 μL) was stereotaxically injected into the SVZ (relative to the bregma: anterior, 0.8 mm; lateral, 1.0 mm; depth, 2.2-1.9 mm) of P7-8 WT mice.

METHOD DETAILS

DNA constructs

To generate pGEX-myc (fused to N-terminal GST-myc tag) vector, DNA fragments: pGEX-myc F (5′-AGATCTGAGCAGAAACT CATCTCTGAAGAGGATCTGGGATCCCCGGAATTC-3′) and pGEX-myc R (5′-GAATTCCGGGGATCCCAGATCCTCTTCAGAGAT GAGTTTCTGCTCAGATCT-3′), were hybridized and inserted into pGEX-6p-1 (GE Healthcare). To generate pGEX-myc-shootin1b, pmRFP-shootin1b, pCMV-FLAG-shootin1b and pCMV-myc-shootin1b, rat shootin1b cDNA (Higashiguchi et al., 2016) was subcloned into pGEX-myc, pmRFP-C1 (Takara), pCMV-FLAG (Agilent Technologies) and pCMV-myc (Agilent Technologies) vectors. To generate pmRFP-N1 (fused to C-terminal mRFP tag) vector, mRFP was amplified by PCR with the primers mRFP F (5′-AAAGAATT CAGATCTGATATCCTCGAGGCCACCATGGCCTCCTCCGAGGACGTCATC-3′) and mRFP R (5′-AAAGGATCCTTAGGCGCCGGTG GAGTGGCGGCCCT-3′), and then subcloned into pEGFP-N1 (Takara). To generate H2B-mRFP and centrin2-mNeonGreen, human H2B and centrin2 were amplified by PCR from a human fetal brain cDNA library (Takara) with the following primers: H2B F (5′-AAACTCGAGGCCACCATGCCAGAGCCAGCGAAGTCTGCT-3′), H2B R (5′-GGGCTCGAGCTTAGCGCTGGTGTACTTGGT GAC-3′), centirn2 F (5′-GGACTCGAGGCCACCATGGCCTCCAACTTTAAGAAGGC-3′), and centrin2 R (5′-TTTGGATCCCGATA GAGGCTGGTCTTTTTCATG-3′); they were then subcloned into pmRFP-N1 and pmNeonGreen-N1 (Allele Biotechnology) vectors, respectively. To generate pFN21A-HaloTag-actin, pFN21A-HaloTag-cortactin and pFN21A-HaloTag-shootin1b, the cDNAs of human β-actin (Katsuno et al., 2015), rat cortactin (Kubo et al., 2015) and rat shootin1b (Higashiguchi et al., 2016) were amplified by PCR with the following primers: actin F (5′-GAGCGATCGCCATGGATGATGATATCGCC-3′), actin R (5′-GGGTTTAAACTGATCAGT TATCTAGATCC-3′), cortactin F (5′-ATATGCGATCGCCATGTGGAAAGCTTCT-3′), cortactin R (5′-ATATGTTTAAACCTGCCG CAGCTCCAC-3′), shootin1b F (5′-ATATGCGATCGCCATGAACAGCTCGGA-3′) and shootin1b R (5′-GGGTTTAAACTCAGCAGTTA GAACTGTC-3′); they were then subcloned into pFN21A HaloTag CMV Flexi vector (Promega). Construction of pCAGGS-myc-NES-GST, pCAGGS-myc-NES-shootin1 (261-377) and pCMV-FLAG-cortactin were described previously (Shimada et al., 2008; Kubo et al., 2015). To generate pCAGGS-EGFP-NES, the DNA fragments EGFP-NES F s(5′-GATCACTTGCACTTAAACTGGCTG GACTTGACCTGA-3′) and EGFP-NES R (5′-GATCTCAGGTCAAGTCCAGCCAGTTTAAGTGCAAGT-3′) were hybridized and inserted into pCAGGS-EGFP vector (Baba et al., 2018). To generate pCAGGS-EGFP-NES-shootin1 DN, human shootin1 (261-377) cDNA (Kubo et al., 2015) was subcloned into pCAGGS-EGFP-NES.

Histological analysis

For immunohistochemistry, mouse embryos and P0 mouse brains were fixed with 4% PFA for 1 h and 6 h, respectively. PFA was replaced with 30% sucrose in PBS for overnight at 4°C, and then frozen in Tissue Tek optimal cutting temperature (OCT, Sakura Finetek). Tissue blocks were cut into sagittal sections of 12 μm thickness using a cryostat (NX70, Micro-edge Instruments). The sections were incubated with blocking solution [10% normal goat serum (Vector Laboratories) and 0.3% Triton X-100 (Wako) in phosphate buffer] for 2 h at room temperature. After blocking, they were incubated with primary antibody diluted with the blocking solution for overnight at 4°C. They were washed with phosphate buffer containing 0.3% Triton X-100 (PBT buffer) and incubated with secondary antibody and 1 μg/ml 4′, 6-diamidino-2-phenylindole (DAPI) diluted with blocking solution overnight at 4°C. They were then washed with PBT buffer and mounted with ProLong Gold (Thermo Fisher Scientific). The following primary antibodies were used: rabbit anti-shootin1a (Baba et al., 2018) (1:1000), rabbit anti-shootin1b (Higashiguchi et al., 2016) (1:5000), rabbit anti-Tbr2 (1:1000, Abcam). The secondary antibody used was Alexa Fluor 594-conjugated donkey anti-rabbit (1:1000, Thermo Fisher Scientific). Fluorescence images were acquired using a confocal laser microscope (LSM710, Carl Zeiss) equipped with a Plan-Apochromat 20x, 0.8 numerical aperture (NA) objective lens (Carl Zeiss) and imaging software (ZEN2009, Carl Zeiss).

For Nissl staining, P0 mouse brains were fixed with Bouin solution (Wako) overnight at 4°C. Fixed brains were embedded in paraffin and cut into sagittal sections of 12 μm thickness using a microtome (HM340E, Micro-edge Instruments). Sections were stained with 0.1% thionine (Wako). Images were acquired using an upright microscope (BX43, Olympus) equipped with a Plan Apo N 1.25x, 0.04 NA objective lens (Olympus).

Immunocytochemistry

Cultured cells were fixed with 4% PFA dissolved in Krebs buffer for 15 min on ice for immunocytochemistry as described previously (Kubo et al., 2015), except for phalloidin staining. For phalloidin staining, cells were fixed with 4% PFA dissolved in PBS for 10 min at 37°C. The cells were treated with 0.05% Triton X-100 in PBS for 15 min on ice and 5% bovine serum albumin (BSA, Sigma) in PBS for 1 h at room temperature, and then incubated with primary antibody diluted in PBS containing 5% BSA overnight at 4°C. They were washed with PBS, and then incubated with secondary antibody diluted in PBS overnight at room temperature. After washing with PBS, they were stained with Alexa Fluor 594-conjugated phalloidin (1:100, Thermo Fisher Scientific) for 30 min at room temperature. We used a 1:1 mixture of glycerol (Nacalai Tesque) and PBS as a mounting solution. Fluorescence images were acquired using either a fluorescence microscope (Axioplan2, Carl Zeiss) equipped with a Plan-Neofluar 63x oil, 1.40 NA objective lens (Carl Zeiss), a charge-coupled device camera (CCD, AxioCam MRm, Carl Zeiss) and imaging software (Axiovision3, Carl Zeiss), or a TIRF microscope (IX81, Olympus) equipped with an EM-CCD camera (Ixon3, Andor), a UAPON 100x, 1.49 NA (Olympus) and imaging software (MetaMorph, Molecular Devices). The following primary antibodies were used: rabbit anti-shootin1a (1:10000) (Baba et al., 2018), rabbit anti-shootin1b (1:20000) (Higashiguchi et al., 2016), mouse anti-cortactin (1:500, Millipore), goat anti-doublecortin (1:1000, Santa Cruz Biotechnology) and goat anti-L1 (1:1000, Santa Cruz Biotechnology). The following secondary antibodies were used: Alexa Fluor 594-conjugated donkey anti-rabbit (1:1000, Jackson ImmunoResearch), Alexa Fluor 488-conjugated goat anti-rabbit (1:1000, Thermo Fisher Scientific), Alexa Fluor 488-conjugated donkey anti-goat (1:1000, Thermo Fisher Scientific) and Alexa Fluor 488-conjugated goat anti-mouse (1:1000, Thermo Fisher Scientific). For 7-amino-4-chloromethylcoumarin (CMAC, Thermo Fisher Scientific) staining, cells were incubated with 5 μM CMAC for 2 h at 37°C before fixation.

Preparation of brain lysate and HEK293T cell lysate

Lysates of E19 rat or E18 mouse brains were prepared as described previously (Toriyama et al., 2006). E19 rat brain lysate was used for immunoprecipitation, while E18 mouse brain lysate was used for Figure 2A. Lysates of HEK293T cells were prepared as described previously (Baba et al., 2018).

Immunoprecipitation and Immunoblotting

Immunoprecipitation and immunoblotting were performed as described previously (Shimada et al., 2008; Baba et al., 2018). The following primary antibodies were used in immunoblotting: rabbit anti-shootin1 (Toriyama et al., 2006) (1:500), rabbit anti-shootin1a (Baba et al., 2018) (1:10000), rabbit anti-shootin1b (Higashiguchi et al., 2016) (1:20000), mouse anti-cortactin (1:500, Millipore), goat anti-L1 (1:1000, Santa Cruz Biotechnology), rabbit ant-myc tag (1:2000, MBL), mouse anti-actin (1:10000, Millipore), rabbit anti-GFP (1:2000, MBL), mouse anti-FLAG (DDDDK) tag (1:4000, MBL). The following secondary antibodies were used in immunoblotting: HRP-conjugated donkey anti-rabbit IgG (1:2000, GE Healthcare), HRP-conjugated goat anti-mouse IgG (1:5000, Thermo Fisher Scientific) and HRP-conjugated donkey anti-goat IgG (1:2000, Millipore).

Protein preparation

Recombinant proteins were expressed in *Escherichia coli* as GST fusion proteins and purified on Glutathione Sepharose columns (GE Healthcare), after which GST was removed by PreScission protease (GE Healthcare) as described (Kubo et al., 2015). L1-CAM-Fc was prepared as described (Kubo et al., 2015).

In vitro binding assay

Purified 100 nM myc-shootin1b was mixed with 12.5 μL (bed volume) of anti-myc tag mAb magnetic beads (MBL) and rotated for 1 h at 4°C in reaction buffer (20 mM Tris-HCl pH 8.0, 100 mM NaCl, 1 mM EDTA, 1 mM DTT). Magnetic beads were separated from the supernatant using a magnetic rack and washed with wash buffer (reaction buffer containing 0.1% Nonidet P-40 (NP-40, Nacalai Tesque). After the supernatant was removed, the beads were mixed with purified 100 nM cortactin or L1-CAM-ICD (L1-CAM intracellular domain) and rotated for 1 h at 4°C in reaction buffer. The beads were washed with wash buffer, and immunocomplexes were then analyzed by immunoblotting.

Time-lapse imaging of cells in Matrigel

Before observation, the culture medium was replaced with L-15 medium containing 2% B-27 supplement and 1 mM glutamine. Phase contrast and fluorescence images were acquired at 37°C using a fluorescence microscope (IX81, Olympus) equipped with Plan Fluar 40x, 0.60 NA (Olympus) or Plan SApo 40x, 0.95 NA, an electron multiplying-CCD camera (EMCCD, iXon DU888, Andor) and MetaMorph. Phase contrast and fluorescence images were acquired every 2 min for 3 h and 2 h, respectively. For experiments in Figure 4C, neuroblasts were transfected with pAcGFP, and some of them were co-transfected with pCMV-FLAG-shootin1b; AcGFP fluorescence was used as an indicator of transfected cells. For experiments in Figure 7C, neuroblasts were co-transfected with overexpression vectors and pAcGFP; AcGFP fluorescence was used as an indicator of transfected cells.

Somal translocation speed was analyzed by tracing the soma during observation. Neuroblasts that reversed their migratory direction during observation were eliminated from the analyses. For calculating the length of the leading process (Figures 4D, 4G, and 4H and Figures 7F and 7G) and the distance between centrosome and nucleus (Figures S4B, S4D, and S4E), the quantified data were smoothed by $\overline{x}(t) = 1/5 \sum_{k=-2}^{2} x(t+k)$ to reduce noise, where x is length (μm) and t is time (min), respectively. The calculated length and distance show dynamic fluctuations (Figures 4D and S4B). Peaks and troughs are indicated by red and blue arrowheads, respectively. Data in Figures 4G, 7F, and S4D were obtained by averaging the difference between peak and trough, while those in Figures 4H, 7G, and S4E were calculated by averaging the number of peaks and troughs.

Analysis of neuronal migration in fixed brain slices

Two days after SVZ cell transplantation (P9-10), the animals were deeply anesthetized and perfused transcardially with PBS, followed by 4% paraformaldehyde (PFA) in 0.1 M phosphate buffer. The fixed brains were cut into sagittal slices (60 μm thick) using a vibratome (VT1200S, Leica). After nuclear staining with Hoechst 33342 (1:5000, Thermo Fisher Scientific), z stack images of the sections containing the entire RMS were obtained using an inverted confocal microscope (LSM700, Carl Zeiss). The numbers of PKH-labeled cells distributed in pRMS, aRMS, OB-RMS and OB-outer (Figure S3) in these images were counted.

Time-lapse imaging of neuronal migration in brain slices

Brain slices for time-lapse imaging were prepared 2 days after the cell transplantation (P9-10), as reported previously (Kaneko et al., 2010), with modifications. Briefly, dissected brains were cut into sagittal slices (200 μm thick) using a vibratome (VT1200S, Leica). The slices were cultured on a filter membrane (Millipore) submerged in Neurobasal medium supplemented with 10% FBS, 2% B-27 supplement, 2 mM L-glutamine and 50 U/ml penicillin-streptomycin. Images were acquired using an inverted confocal microscope (LSM710, Carl Zeiss) equipped with a gallium arsenide phosphide detector and a stage top microscope incubator (5% CO_2 at 37°C, Tokai Hit), z stack (10 z sections with 8-10 μm step sizes) images were acquired every 6 min for 8-14 h. To quantify the migration speed of neuroblasts with a monopolar or bipolar shape in the RMS, these cells were traced using ImageJ software (manual tracking plugin). Only those neuroblasts that could be continuously tracked for at least 40 min were used for this analysis.

Fluorescent speckle imaging

Speckle imaging was performed as described previously (Shimada et al., 2008). For experiments in Figures 6D–6F, 6I, and 7A, neuroblasts cultured on laminin-coated or on L1-CAM-Fc-coated glass bottom dishes were treated with HaloTag TMR ligand (Promega) at 1:2000 dilution in the culture medium and incubated for 1 h at 37°C. The ligand was then washed out with PBS and the cells were incubated in L-15 medium containing 2% B27 supplement and 1 mM glutamine. The fluorescent speckles were acquired using a fluorescence microscope (AxioObserver Z1, Carl Zeiss) equipped with a complementary metal oxide semiconductor camera (CMOS, ORCA Flash4.0 V2, Hamamatsu), a Plan-Apochromat 100x, 1.40 NA (Carl Zeiss) and imaging software (ZEN2012, Carl Zeiss). Fluorescence images were acquired every 3 s for 150 s.

Traction force microscopy

Acrylamide gels containing 200 nm fluorescent beads were prepared as described (Toriyama et al., 2013). SVZ explants in a mixture of 75% Matrigel and 25% L-15 medium were plated on the L1-CAM-Fc-coated acrylamide gel and incubated at 37°C for 30 min to solidify the Matrigel, and then cultured with Neurobasal medium containing 2% B-27 supplement and 1 mM glutamine in a humidified, 5% CO_2, 37°C incubator. Images were acquired every 30 s for 24.5 min. Magnitude and angle of the traction force under the cells were calculated as described previously (Toriyama et al., 2013).

QUANTIFICATION AND STATISTICAL ANALYSIS

All data are shown as the mean ± SEM. All statistical analysis were performed using Excel 2016 (Microsoft) and GraphPad Prism7 (GraphPad Software). Significance was determined by the two-tailed paired t test, unpaired Student's t test or unpaired Welch's t test. For multiple comparisons, we used one-way ANOVA with Tukey's post hoc test. For each experiment, the corresponding statistics information and number of samples are indicated in the figure legend. A P value less than 0.05 was considered to be statistically significant.

DATA AND SOFTWARE AVAILABILITY

All software was commercially or freely available, and is listed in the STAR Methods and Key Resources Table. The data that support the findings of this study are available from the corresponding author upon request.